

Article

Not peer-reviewed version

---

# Analysis of the Rolling Phenomenon of a Reduced-Diameter Wheel for Freight Wagons, as a Function of Operating Factors

---

[David S. Pellicer](#) \* and [Emilio Larrodé](#)

Posted Date: 13 August 2024

doi: [10.20944/preprints202408.0896.v1](https://doi.org/10.20944/preprints202408.0896.v1)

Keywords: mathematical modeling; vehicle-track interaction; freight transport; sustainable transport; rail motorway



Preprints.org is a free multidiscipline platform providing preprint service that is dedicated to making early versions of research outputs permanently available and citable. Preprints posted at Preprints.org appear in Web of Science, Crossref, Google Scholar, Scilit, Europe PMC.

Copyright: This is an open access article distributed under the Creative Commons Attribution License which permits unrestricted use, distribution, and reproduction in any medium, provided the original work is properly cited.

Disclaimer/Publisher's Note: The statements, opinions, and data contained in all publications are solely those of the individual author(s) and contributor(s) and not of MDPI and/or the editor(s). MDPI and/or the editor(s) disclaim responsibility for any injury to people or property resulting from any ideas, methods, instructions, or products referred to in the content.

Article

# Analysis of the Rolling Phenomenon of a Reduced-Diameter Wheel for Freight Wagons, as a Function of Operating Factors

David S. Pellicer \* and Emilio Larrodé

Department of Mechanical Engineering, University of Zaragoza, 50018 Zaragoza, Spain

\* Correspondence: dasapezu@unizar.es

**Abstract:** This paper shows the development of a numerical analysis model which enables the calculation of the life of a reduced-diameter wheel used for freight wagons as a function of its operating factors. Reduced-diameter wheels are being increasingly used for combined transport applications and they can be arranged in a wide range of bogies and operated very differently. Due to the uniqueness of this type of wheels, their life has hardly been analyzed so far. To properly construct the numerical analysis model, it has been necessary to study the rolling phenomenon in-depth, tackle the main problems arising in the vehicle – track interaction and set the relations amongst them. Once the rail-wheel interaction model was built, it was used to calculate the life of an ordinary-diameter wheel, a medium-diameter wheel and a reduced-diameter wheels under the same conditions and compare them. In this way, it is possible to know how long the life of a reduced-diameter wheel is compared to that of an ordinary-diameter one and also the evolution of the life depending on the diameter. The root causes responsible for this evolution can be explained thanks to the comprehension of the rolling phenomenon provided by the full analytical work.

**Keywords:** mathematical modeling; vehicle-track interaction; freight transport; sustainable transport; rail motorway

## 1. Introduction

The objective of this work is to tackle the wear problem for reduced-diameter wheels, which presumably do not undergo the same degradation as the ordinary-diameter wheels due to its greater angular contact (number of revolutions) with the rail for the same linear distance traveled (mileage). For that, a calculation model able to determine the life of a wheel as a function of the most significative operating factors, such as the nominal wheel diameter, is developed.

Nowadays, the needs in the field of logistics are changing and new transportation models are arising. One of the models that is becoming more popular in the last years is the rail motorway model, which consists in transporting whole freight articulated vehicles on railway wagons. This model cuts down CO<sub>2</sub> emissions, saves fuel, reduces road congestion and may be more profitable than road transportation for some routes. It can also be used to skip certain obstacles, harsh routes or remote-access zones (Fomento, 2018). The concept of loading the whole heavy-duty vehicle avoids breakbulk shipping whereas it brings the loading and unloading time down to 1 minute, since the vehicles can run on / off board the wagons quickly and then their wheels are secured quickly as well (Jaro & Folgueira, 2012). Figure 1 shows a schematic diagram of this concept:



**Figure 1.** Concept described above. Source: Own elaboration. .

Notwithstanding, the adoption of this model often encounters the problem of loading gauge. Due to the height of the articulated vehicles used for road transportation, around 4 m (European Council, 1996), placing them on wagons leads to a further height increase over the rails that may conflict with the height limitations found in some tunnels or under some overpasses. Figure 2 illustrates this conflict: the European and Spanish loading gauges and their possible interferences with a rail motorway service:

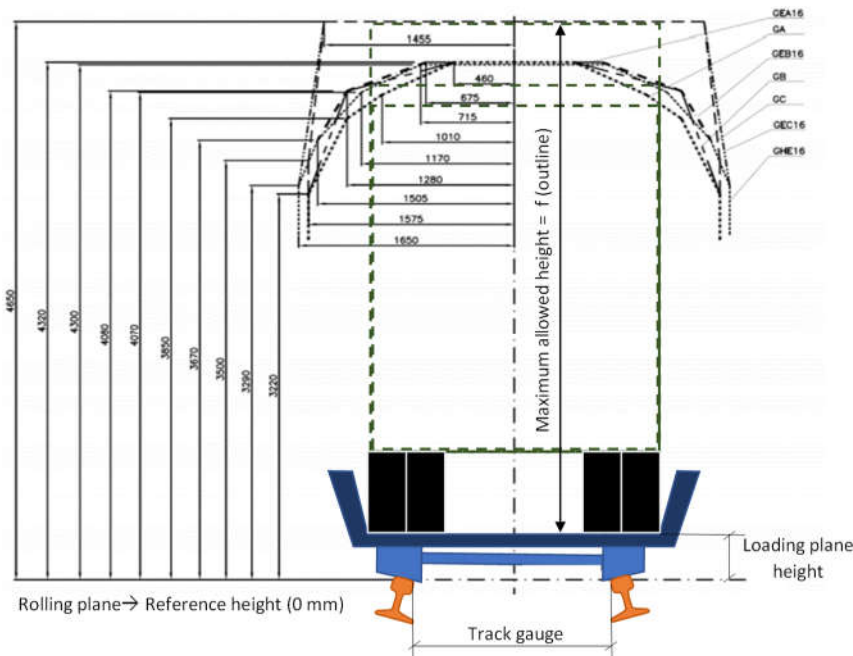


**Figure 2.** Illustration of the described conflict. Source: Modification of a diagram from (Fomento, 2015).

In order to avoid interferences between the load (the heavy-duty vehicles) and the civil structures (tunnels and overpasses found in the railway route) and keep transporting those road vehicles, there is one economically-feasible alternative, as it does not require any civil works on the route: lowering the loading plane height. As it can be seen in Figure 2, this height depends on the wheel diameter among other factors, so it can be lowered by using reduced-diameter wheels (Jaro & Folgueira, 2012).

An ordinary wheel has about 920-mm diameter, while a reduced-diameter wheel has a diameter value between half and third of the ordinary one. This newly poses a problem: If a wheel whose diameter has been halved must roll the same distance as an ordinary-diameter wheel, then the former will have to revolve twice around its rotation axis. Also, its contact angle with the rail will be higher due to its smaller size and it will have less material to support and withstand the same load. Taking this into account, it can be foreseen that the reduced-diameter wheel is likely to experience a more intense wear and rolling contact fatigue (RCF) than the ordinary-diameter wheel. However, this is only a prediction and must be proved and validated mathematically.

For that, the calculation model sought must take into account many railway factors involved in vehicle – track interaction. These parameters can be grouped into four groups:

- Wheel factors: Geometry (diameter, conicity, tread width, contact angle), machining (roughness), material (properties), load and previous wear.
- Wagon factors: Configuration (bogies or axles distribution and type of bogies), type of suspension, braking system, running speed and load distribution (axle load).
- Railway superstructure factors: Track gauge, line layout (curve radii, windiness, sagitta, gradient, etc.), layout quality (excess or deficiency in cant, transition curves, etc.), type of rail (welded or with joints), track materials (properties) and track previous degradation (previous rail wear, specially).

- External factors: Temperature, humidity, wind, rain, snow and weather in general. The presence of moisture, leaves and pollutants (saltpeter, oil, etc.) is in here too.

The process consists of defining a mathematical model under the behavioral equations extracted from the models that can explain wheel degradation, each of which includes a set of hypotheses. The analytical model should have to include as many influence factors as possible; however, the model size must be restricted for it to be computationally – efficient. That implies that additional hypotheses will be formulated in order to take out those factors with a lesser influence on wheel degradation.

Regarding the vehicle, the infrastructure and their interaction, the work aims to focus on the Spanish conventional railway network. This is because rail motorways are currently being fostered in Spain and this country presents some obstacles to their implementation: the conventional railway network presents an unfavorable loading gauge (Fomento, 2018), which prompts the adoption of reduced-diameter wheels, and, additionally, the tight curves and the steep gradients inflict severe damage to wheels. These wheels are arranged in wheelsets, with a wheelset being the rigid union of an axle with a pair of wheels. Wheelsets are usually arranged in two-axle (two-wheelset) bogies and, according to the same Ref., two bogies are enough for a flat-bed wagon used on a rail motorway, so this is the type of railway vehicle that is to be considered for wheel degradation.

With that being said, the analysis will be limited to freight transport and to the Spanish national railway network, whose track gauge is specific: 1,668 mm. The analysis will exclude the aforementioned external factors, as these are fairly volatile and difficult to forecast.

This research paper can be compared to other cutting-edge work on wheel wear calculation, but differs in some significant respects. These differences are commented upon next: To start with, Refs. (Cai et al., 2019), (Chunyan et al., 2024), (Ma et al., 2021) and (Tao et al., 2020) focus on polygonal wheel wear, which is a relevant problem in high-speed railway lines, but they do not include RCF and abrasive-adhesive wear, which so much trouble cause in rail freight transportation. Ref. (Salas & Pascual, 2019) correlates RCF and abrasive-adhesive wear through analytical models and backs up the results experimentally, although it does not give insight into wheel life, not even for ordinary-diameter wheels. Ref. (Sang et al., 2024) is very specific as it focuses on the wheel wear caused under different braking modes, without covering the wear appearing when the vehicle is not braking. Refs. (Lyu et al., 2020) and (Sui et al., 2021) are very specific as they focus on the effect of wheel diameter difference, that is, when the wheels in a wheelset do not have the same diameter, and wheel life is not studied (only numerical simulations and experiments for 200,000 km). Refs. (Pires et al., 2021) and (Zeng et al., 2022) focus on the optimization of the reprofiling cycles for wheels, although their diameter is not varied and the strategy is drawn up only for ordinary-diameter ones. Ref. (Montenegro & Calçada, 2023) develops a wheel – rail contact model which considers many structural elements of the vehicle and the infrastructure; however, it does not consider reduced-diameter wheels either. To end with, Ref. (Bossò et al., 2022) reviews as many numerical models for rail – wheel contact as possible, while Ref. (de Paula Pacheco et al., 2023) compares different wear indicators for quantifying wheel wear in rail freight operations; even so the former does not discuss about numerical models for reduced-diameter wheels and the latter does not apply the wear indicators to them.

The main contribution of this work consists in tackling the physical problem of wear for reduced-diameter wheels, which has been hardly treated due to the uniqueness of this type of wheels. Wheel, wheelset and bogie kinematics and dynamics have been studied in-depth, which makes the work insightful as it provides comprehension as to why wheel life is not the same regardless of its diameter and why a dependency exists.

Differently to the previous research, several realistic scenarios basing on rail motorways have been proposed and the wheel diameter has been varied in the procedure of analysis developed, keeping the rest of the procedure the same or with equivalent parameters, which makes comparisons at the same level possible.

Once the analysis procedure has been validated, the methodology is open to changes, so that other factors can be altered, more factors can be added or some of the behavioral laws can be modified or swapped in future research works.

To conclude with the introduction, it is worth remarking that in order to carry out this research work it has been necessary to review many analytical models which enable the calculation of wheel wear. Some of these models are based on the kinematics of the rolling phenomenon, while others are based on its dynamics. The most recurring Refs. are (Fissette, 2016), (Larrodé, 2007), (Moody, 2014), (Pellicer & Larrodé, 2021), (Oldknow, 2015), (Ortega, 2012), (RENFE, 2020), (Rovira, 2012) and (Sichani, 2016). It is worth mentioning that (Pellicer & Larrodé, 2021) serves as a guide as it reviews the models and bridges the gaps between them by creating mutual interconnections and doing numerical checks when necessary. Additionally, those standards expedited by the Spanish normalization agency (AENOR) and the Spanish railway infrastructure manager (ADIF) which are applied to the field of rail – wheel interaction have also been taken into account so as to collect real data and know the restrictions imposed by these regulations.

## 2. Materials and Methods

This work follows a deductive method, as explained next:

First, the rail – wheel contact problem has been studied basing on the contact friction mechanics theory and the works and studies conducted since the second half of the 18th century.

Second, the contact models have been assessed regarding two criteria: accuracy and computational effort. Those with a higher accuracy and a lower computational cost have been chosen: Hertz's solution, Polach's method, center of friction, energy transfer and fatigue index.

Afterwards, the chosen models have been applied to tackle the main problems arising in the vehicle – track interaction. For this application, the vehicle – track interface has been parametrized, which means that the factors involved in the said interaction have been assigned parameters.

These models include their own application hypothesis, but additional hypotheses are required in order to delimit the problem, so a series of hypotheses have been proposed. These hypotheses are fundamental to include important aspects or discard aspects that will not have a significant impact on the problem solution.

Each of this models consists of a set of equations, which can be used to interrelate the models, so it is possible to construct a numerical analysis model in the form of an algorithm thanks to the existing links and adding new links (geometrical and other mathematical relations, for instance). This algorithm is programmed on mathematical equation solving software, which allows solving all of the equations after inputting the data required.

Then the results are obtained: they come in the form of wear depth of each wheel on a proposed bogie, but the appearing of RCF can be predicted as well. When the wear depth reaches a fixed limit on a wheel, then all of the bogie wheels are reprofiled with a lathe and the wear cycle starts over (the algorithm is run again). It is noteworthy that the parameters of interest, such as the nominal wheel diameter, can be varied at will.

Finally, the results for wheels of different diameter wheels are compared and conclusions upon their behavior and the diameter influence are drawn.

### 2.1. List of Abbreviations

The abbreviations used in the article can be consulted in Table A1 for those with Latin symbols (Appendix A) and Table A2 for those with Greek symbols (Appendix A).

### 2.2. Hypotheses

The following hypotheses have been regarded besides the application hypotheses of Hertz's solution, Polach's method and wear calculation:

- The procedure is based on global calculations for the contact patch, without discretizing it into finite elements.
- It is stationary, that is, it does not consider the variation of variables over the time. At transition curves, where these variations are greater, mean values are computed.

- (c) It disregards any rail wear and it does not consider the previous wheel wear either (it does not update the contact parameters as the profile wears out, but this profile is assiduously renovated).
- (d) It is applied on all of the bogie wheels. For each wheel, the parameters and wear calculations are separately saved. This is because the wear is not the same for all of the wheels mounted on the same bogie (Rovira, 2012).
- (e) It is applied on one bogie belonging to a wagon. A wagon normally consists of two bogies, but they can mostly rotate independently with respect to the other.
- (f) It disregards the tractive and compressive forces that some wagons transmit to the next ones through couplings when curving, which is due to the existing coupling slacks (Moody, 2014).
- (g) It can consider up to 2 contact patches at the same wheel: one of them on the tread and the other on the flange. The load percentage of each patch will be controlled by means of a parameter (Pellicer & Larrodé, 2021).
- (h) In Kalker's and Polach's equations, the spin is assumed to be positive when it is clockwise, as it must comply with the sign convention applied for creepage. This spin is later passed on to the energy transfer model employed.
- (i) Creepage is obtained from a kinematic analysis of the wheelsets rather than from the non-dimensional slips (these include partial derivatives which are usually not applied to global calculations).
- (j) In the whole study, the radial deformation  $\delta_o$  is disregarded with respect to the wheel radius  $r_o$  (this is a usual hypothesis in these studies because  $\delta_o \ll r_o$ ).
- (k) As  $\Phi \ll \gamma_o$  (in fact,  $\Phi \ll \psi \ll \gamma_o$ , judging by the values obtained in (Pellicer & Larrodé, 2021)), the effect of  $\Phi$  on  $\gamma_o$  can be disregarded as well.
- (l) In contrast, the effect of  $\Phi$  on the wear happening at transition curves is not considered, given that it increases the wear slightly.
- (m) In this kinematic analysis, the displacements from bogie suspensions and anti-yaw are not included.
- (n) The variation of the wheel and rail curvatures at transition curves is discarded, given that, although the location of the rail-wheel contact varies along the wheel and rail widths (and their curvatures as a consequence), these variations are usually very small. When these variations are great, the most unfavorable values are directly taken (for instance, the curvatures of flange-rail contact when this contact is predicted to appear at a certain transition curve).
- (o) Only abrasive and adhesive wear are considered, without considering defects such as cracks, spalling, squats, flats, etc. (Ortega, 2012), (RENFE, 2020).
- (p) RCF is only predicted, without computing the extent of the damage produced, often sub-surface cracks (Ortega, 2012).
- (q) The bogie wheels are considered to be non-powered, so  $F_t = 0$  at the wheel-rail interfaces.
- (r) The bogie wheels are considered to be equipped with disk brakes, which do not wear the wheels out (Pellicer & Larrodé, 2021).
- (s) The railway vehicle is presumed to negotiate curves (circular or transition ones) at a constant speed, so it brakes (if necessary) before negotiating them, so  $F_f = 0$  at a curve. There is an exception when the vehicle is running downhill, as explained in the next hypothesis.
- (t) The railway vehicle is assumed to brake slightly when running downhill and reducing or cutting off traction is not enough to keep a constant speed at curves: when the slope is less than 10 %, the vehicle brakes will be off, when the slope is between 10 and 15 %, the brakes will brake 5 % of the accelerating force at each wheelset, and when the slope is greater than 15 %, the brakes will brake 10 % of the accelerating force.
- (u) The infrastructure parameters that modify the wear conditions, such as warp, rail deflection, joints, impacts against switch frogs and track devices and track irregularities are not considered (Larrodé, 2007).
- (v) The influence of manufacturing or assembly tolerances of any element is not considered.

- (w) By not considering rail deflection or manufacturing and assembly tolerances, it is possible to assume that the longitudinal rail curve radius ( $R_{y,1}$ ) tends to infinity, so that the associated curvature ( $1/R_{y,1}$ ) tends to zero and can be taken as such.
- (x) The bogie wheels are assumed not to derail or block (this was numerically verified in (Pellicer & Larrodé, 2021)). Also, and they are assumed not to displace laterally under cant deficiency or excess and low static friction conditions (Pellicer & Larrodé, 2021).
- (y) There is not any hunting oscillation at the speed ranges considered (this was numerically proven in (Pellicer & Larrodé, 2021)).

### 2.3. Calculation Process

An algorithm consisting of input data blocks, calculation blocks and two output blocks has been constructed and is shown in Figure 3. Each of the equation blocks textually described is linked with its corresponding document title, under which it is described in detail:

- At the top of the algorithm, the input data is entered to the calculation blocks. The data is arranged in blocks that are added before going down to the main branches. These blocks gather information on the wheelset and bogie geometry, vehicle speed, railway line geometry, wheel geometry, load characteristics, rail geometry and contact materials properties.
- On the left, in the 3 central blocks, the kinematic parameters for the wheelsets are obtained through relations dependent on the line geometry after inputting information on the wheelset and bogie geometry, vehicle speed, railway line geometry and wheel geometry. After that, the uncentering of each wheelset is saturated through equations dependent on the line geometry and, finally, creepages are obtained through kinematics equations.
- On the right, in the 6 central blocks, the normal force on each wheel is computed by means of dynamics equations after entering data on the vehicle speed, line geometry, load characteristics and some results coming from the left main branch after the saturation of uncentering. Afterwards, the geometric and normal contact problems are solved by means of Hertz's solution, for which data on the wheel and rail geometries and the contact materials properties is needed. The results of Hertz's solution and the creepages computed in the left main branch allow applying Polach's method. This solution can be applied either with constant or variable friction. At the end of this branch, the flange – rail contact is characterized by means of equilibrium equations.
- At the bottom of the algorithm, the wheel wear is computed through the energy transfer model and the appearing of RCF is predicted with the fatigue index model.

In Figure 3, input data blocks are represented in green, intermediate equation blocks are shown in blue (light for kinematics and dark for dynamics) and the output blocks are in purple. As to the symbols, the orange one with a diagonal cross inside represents the addition of values, the orange one with a Greek cross inside indicates a disjunctive, the gray one indicates that only one flow is inputted and, finally, the yellow one a bifurcation:

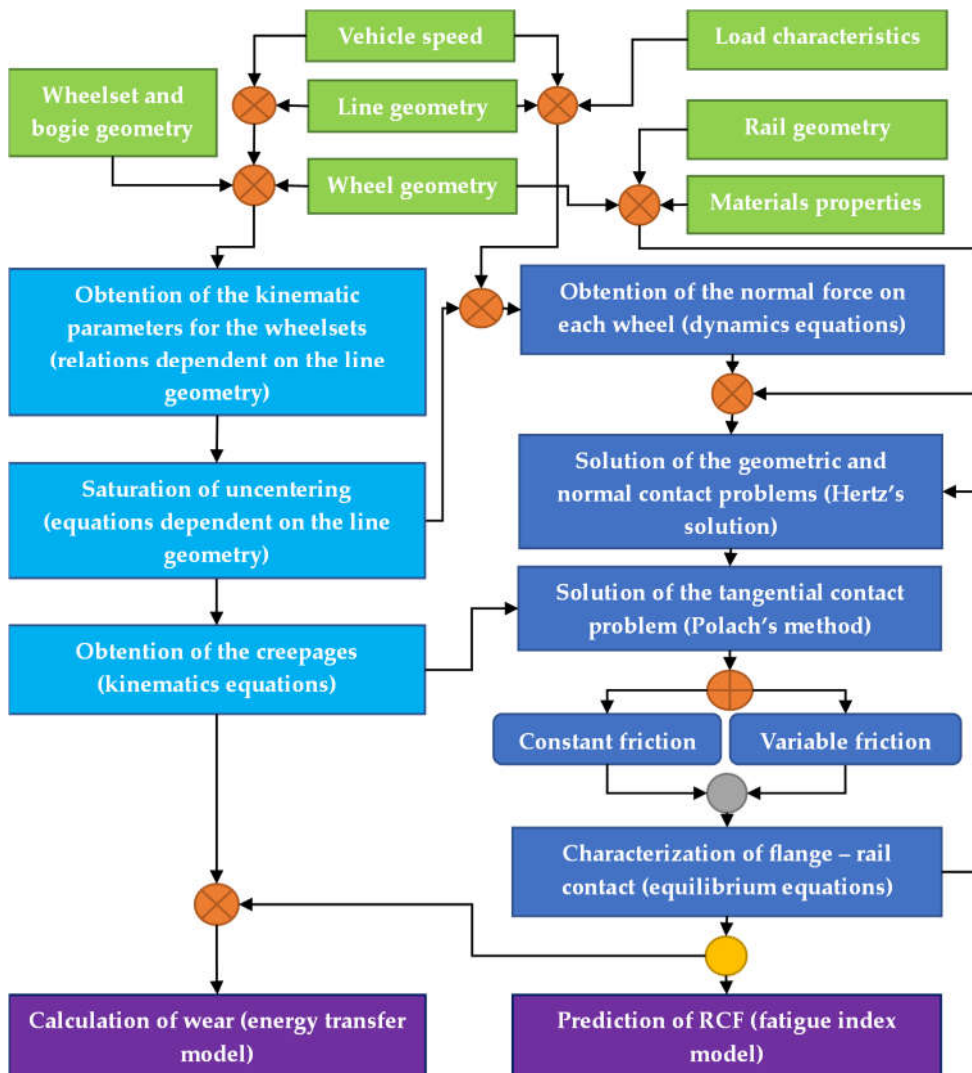


**Figure 3.** Flow diagram of the calculation process (algorithm). Source: Own elaboration.

In this way, it is ensured that the equations that allow calculating wheel wear and predicting RCF are fulfilled under all the requirements and considering all the starting hypotheses, with which the physical phenomenon is characterized. Once the problem has been formulated, and the equations and the input data have been introduced into the software, the parameters of interest, such as the wheel diameter in this case, are varied according to the simulation procedures and the wear is computed.

#### 2.4. Calculation Model

The calculation model is defined in this subsection, starting with the reference frames definition and following with the mathematical description of each of the equation blocks shown in Figure 3 (Section 2.3). The blocks belonging to the left main branch (those related with kinematics) are presented first, while the blocks of the right main branch (related with dynamics) are presented then.

##### 2.4.1. Reference Frames Definition

Four reference frames have been defined for the kinematics and dynamics analyses described in the next pages. These frames are described below and shown in Figure 4 for a wheelset (for the whole bogie does not need a specific reference frame):

- Absolute reference frame  $XYZ$ , clockwise, fixed and whose origin set on the rolling plane, anchored to the track beginning and centered between the rails.

- Track reference frame  $\tilde{x}\tilde{y}\tilde{z}$ , clockwise, mobile at the vehicle speed and whose origin is set on the rolling plane and along the track middle line, holding the  $\tilde{x}$  axis always tangent to that line.
- Axle reference frame  $\bar{x}\bar{y}\bar{z}$ , clockwise, mobile at the axle speed and whose origin is set at the gravity center of the wheelset.
- Contact area reference frame  $x_c y_c z_c$ , clockwise, mobile at the contact area speed and whose origin is set on the center of the area.

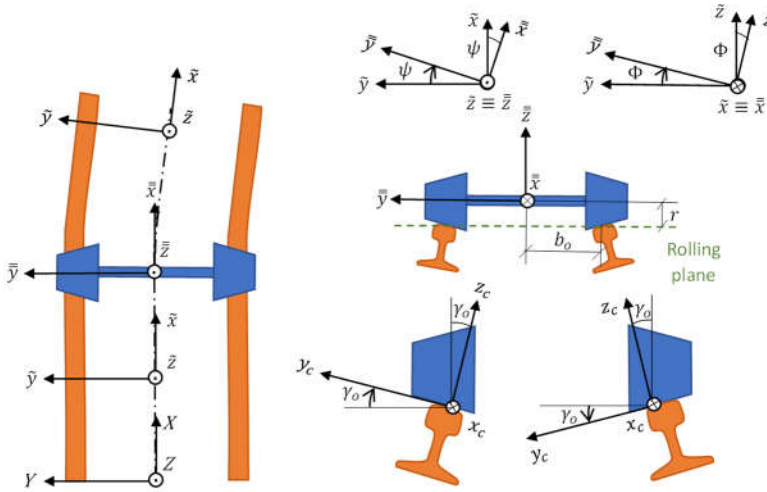


**Figure 4.** Reference frames definition. Source: Own elaboration.

#### 2.4.2. Obtention of the Kinematic Parameters

Refs. (Fissette, 2016), (Moody, 2014), (Oldknow, 2015), (Ortega, 2012), (Rovira, 2012) and (Sichani, 2016) explain how to obtain the kinematic parameters for the wheelsets through relations dependent on the railway line geometry. Not only does Ref. (Pellicer & Larrodé, 2021) collect these relations, but it also extends them to all of the possible geometries that can be found in a railway line:

1. Straight section.
2. Circular curve.
3. Transition curve: Clothoid, quadratic parabola or cubic parabola.

As to the curves, a circular curve is simple that whose radius holds constant, while the transition curves are those whose radii are variable: the radius of a clothoid, also called Euler or Cornu spiral, is inversely proportional to the distance run, while the radii of quadratic and cubic parabolas depend on the distance by those mathematical functions.

The parameters obtained at these geometries are listed next according to the order in which the relations were collected and generalized in Ref. (Pellicer & Larrodé, 2021):

- Uncentering and uncentering speed.
- Average uncentering and uncentering speed.
- Yaw angle and yaw angle variation speed / rate.
- Average sinus of yaw angle and of yaw angle variation.
- Average yaw angle.
- Combination of the uncentering and yaw angle effects.
- Angle of longitudinal displacement of the contact area.
- Tilt and tilt speed / rate.

An example of the parameters obtention is given next: uncentering. This parameter ( $y$ ) can be defined as the distance between the wheelset center of gravity and the track center. Uncentering happens because of wheel conicity: wheels are slightly tapered to make wheel negotiation possible for wheelsets, which lack a differential. In this way, the wheel whose position is inner in relation to the curve can roll with a lower rolling radius than the nominal radius, while the opposite is true for the wheel whose position is outer in relation to the curve, so in the end, the outer wheel rolls a longer distance than the inner one and the wheelset can negotiate the curve with a lower slip.

The uncentering parameter is associated with some track and wheelset parameters, which are shown in Figure 5, except for (equivalent) conicity ( $k$ ), which is an intrinsic parameter of each wheel. These parameters can be interrelated by computing the linear velocities of each wheel and equating them or by applying the Thales's Theorem to the triangles drawn in Figure 5. The formula for uncentering is called after F. J. Redtenbacher, who developed it in the 19th century:

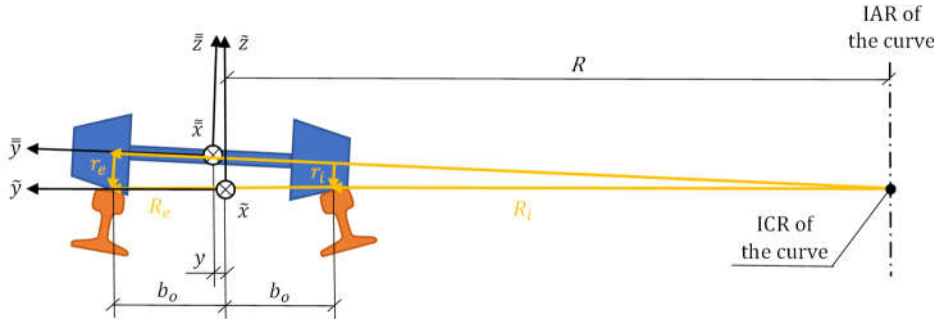


**Figure 5.** Equilibrium position at a curve whose instant center of rotation (ICR) and instant axis of rotation (IAR) are at its right. Source: Own elaboration.

$$y = \frac{r_o b_o}{kR} \quad (1)$$

#### 2.4.3. Saturation of Uncentering

As explained in Refs. (Oldknow, 2015), (Ortega, 2012), (Rovira, 2012) and (Sichani, 2016), the total uncentering of a wheelset ( $y^*$ ) can be computed by adding the original uncentering and the uncentering coming from wheelset rotation (this rotation is in reality that of the bogie pivot with respect to the tangent line to the track centerline). This is shown in Figure 6(a) and the formulae are presented after it.

The reason why uncentering must be saturated is because there exists a geometrical constraint: total uncentering cannot be greater than the addition of half the track play / slack (the so – called "flangeway clearance) and the existing gauge widening (equal or different to 0). When total uncentering reaches that value, then the flange belonging to the outer wheel touches the outer rail. Ref. (Pellicer & Larrodé, 2021) explains this in detail and defines all of the track and wheelset / bogie parameters involved. These parameters are listed below (SC – Parameters are found at straight sections and curves, while C – Parameters are only found at curves under the current hypotheses), most of which are shown in Figure 6(b), and the formulae are presented after it:

- SC – Rolling radius ( $r_o$ ).
- SC – Track gauge ( $J \rightarrow 1,668$  for Iberian gauge).
- SC – Rail inclination ( $1: no \rightarrow 1: 20$  for Iberian gauge).
- SC – Track play / slack ( $\eta$ ).
- C – Curve radius ( $R$ ).
- C – Gauge widening ( $\xi$ ).
- C – Curve sagitta ( $\delta$ ).
- C – Total uncentering ( $y^*$ ) and uncentering limit ( $y_{lim}^*$  or  $y_{lim}$ ).
- C – Outer | inner wheel rolling radius ( $r_e | r_i$ ).
- C – Yaw ( $\psi$ ) and tilt angles ( $\Phi$ ).
- C – Angle of longitudinal displacement of the contact area ( $\zeta$ ).

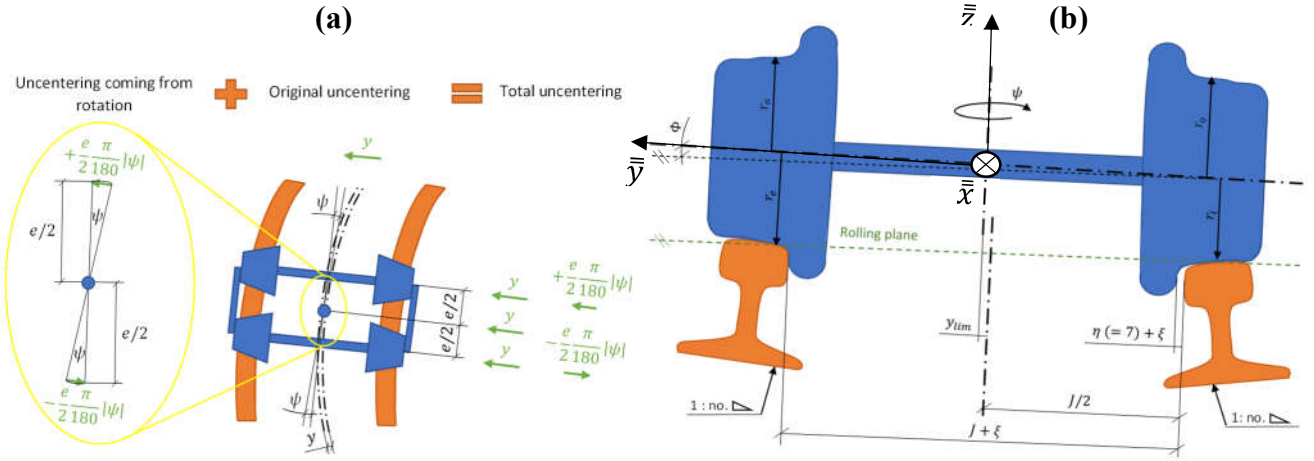


**Figure 6.** (a) Computation of total uncentering by considering the uncentering due to bogie rotation; (b) Wheelset positioning on a narrow curve.

$$y^* \text{ (1}^{\text{st}} \text{ wheelset)} = y + e \frac{\pi |\psi|}{360} \quad (2)$$

$$y^* \text{ (2}^{\text{nd}} \text{ wheelset)} = y - e \frac{\pi |\psi|}{360} \quad (3)$$

$$y_{lim}^* = \frac{\eta}{2} + \xi \quad (4)$$

$$y^* = y_{lim}^* \text{ (if the former was greater before)} \quad (5)$$

#### 2.4.4. Obtention of the Creepages

As explained in Ref. (Sichani, 2016), creepages are the rigid slip velocities divided by the vehicle speed in order to turn them into non-dimensional (although the spin creepage is dimensional as the resulting units are “rad/m”):

$$v_x = \Delta V_x / V \quad (6)$$

$$v_y = \Delta V_y / V \quad (7)$$

$$\varphi = \Phi / V \quad (8)$$

Refs. (Fissette, 2016), (Ortega, 2012) and (Sichani, 2016) explain how to compute creepage from kinematics parameters, whereas Ref. (Pellicer & Larrodé, 2021) collects this information and proves the formulae. The whole process is briefly explained next, starting with longitudinal creepage, continuing with lateral creepage and ending with spin creepage.

Longitudinal creepage has three main contributions, which are represented in Figure 7 and added thereafter:

1. Difference between the nominal wheel radius and the real rolling one (generating  $V_x^I$ ).
2. Application of tractive or braking torques to the wheel (generating  $V_x^{II}$ ).
3. Variation of yaw angle (generating  $V_x^{III}$ ).

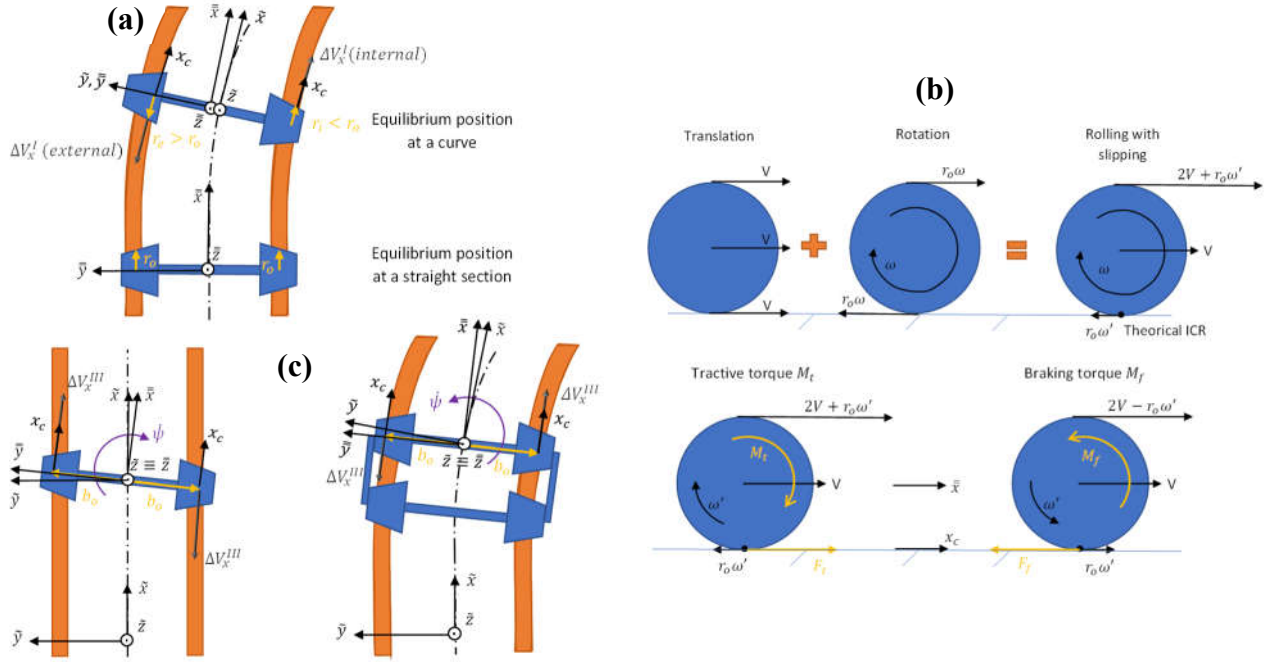


**Figure 7.** (a) First contribution ( $V_x^I$ ); (b) Second contribution ( $V_x^{II}$ ); (c) Third contribution ( $V_x^{III}$ ). Source: Own elaboration.

$$\Delta V_x = V_x^I + V_x^{III} + V_x^{II} \quad (9)$$

$$\Delta V_x = -\Delta r \omega - r_o \omega' \pm b_o \dot{\psi} \quad (10)$$

$$v_x = \frac{-\Delta r}{r_o} + \frac{-r_o \omega' \pm b_o \dot{\psi}}{V} \quad (11)$$

As to lateral creepage, this is composed of three contributions, which are represented in Figure 8 and added thereafter:

1. Not null yaw angle (generating  $\Delta V_y^I$ ).
2. Adoption of a new equilibrium position by the wheelset (generating  $\Delta V_y^{II}$ ).
3. Not null tilt angle (generating  $\Delta V_y^{III}$ ).

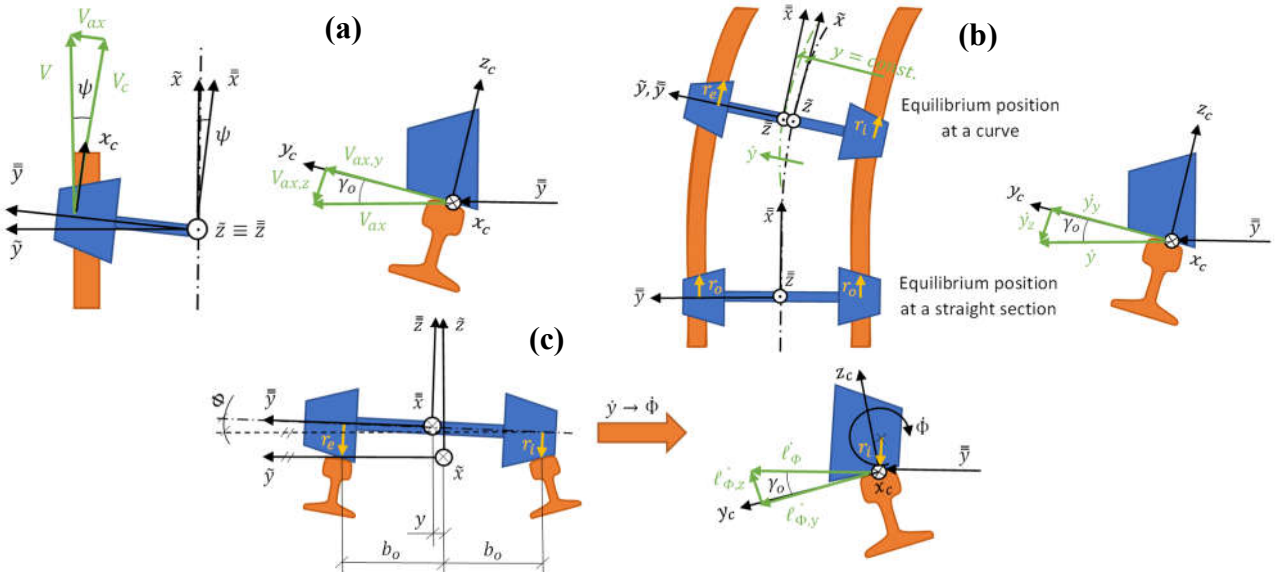


**Figure 8.** (a) First contribution ( $V_y^I$ ); (b) Second contribution ( $V_y^{II}$ ); (c) Third contribution ( $V_y^{III}$ ). Source: Own elaboration.

$$\Delta V_y = V_y^I + V_y^{II} + V_y^{III} \quad (12)$$

$$\Delta V_y = -V \sin \psi \cos \gamma_o + \dot{\gamma} \cos \gamma_o - r_t \dot{\Phi} \cos \gamma_o \quad (13)$$

$$v_y = \left( -\sin \psi + \frac{\dot{\gamma} - r_t \dot{\Phi}}{V} \right) \cos \gamma_o \quad (14)$$

Finally, spin creepage is made up of two contributions, which are shown in Figure 9 and added afterwards:

1. Conicity (generating  $\Delta\Phi^I$ , alternatively known as the camber effect (Ortega, 2012)).
2. Variation of yaw angle (generating  $\Delta\Phi^{II}$ ).

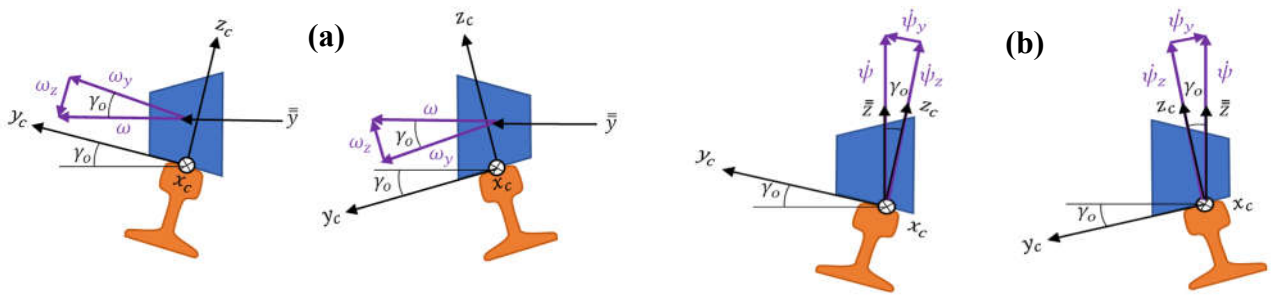


**Figure 9.** (a) First contribution ( $\Delta\Phi^I$ ); (b) Second contribution ( $\Delta\Phi^{II}$ ). Source: Own elaboration.

$$\Delta\Phi = \Delta\Phi^I + \Delta\Phi^{II} \quad (15)$$

$$\Delta\Phi = \pm \omega \sin \gamma_o + \dot{\psi} \cos \gamma_o \quad (16)$$

$$\varphi = \pm \frac{\sin \gamma_o}{r_o} + \frac{\dot{\psi} \cos \gamma_o}{V} \quad (17)$$

#### 2.4.5. Obtention of the Normal Force on Each Wheel

The normal force is exerted by the rail on the wheel as a response to the opposite force (due to gravity or components of accelerations such as the centrifugal one) that the latter exerts on the former. Refs. (ADIF, 1983 – 2021), (ADIF, 2023), (Andrews, 1986), (Fissette, 2016), (Jiménez, 2016), (Ministerio de Fomento, 2018), (Moody, 2014), (Rincón, 2018), (Rovira, 2012), (Santamaría et al., 2009), (Tipler & Mosca, 2014) provide some information on how to compute the normal force on each wheel.

However, the most important Ref. is (Pellicer & Larrodé, 2021), as it is the one which fills the gaps and obtains the normal force on each wheel as a function of these factors:

- Axle load ( $\lambda_{eje}$ ), which obtained from the payload, tare and number of axles.
- Center of gravity of the axle load ( $H_{CdG}$ ), considering the contribution of each load.
- Gradient angle ( $\beta_{rp}$ ), which is directly inferred from the inclination ( $i$ ).
- Cant angle ( $\vartheta_r$ ), which depends on the cant and the distance between contact areas.
- Lateral acceleration ( $a_{lat}$ ), which considers the effect of cant excess or deficiency.
- Wheel contact angle ( $\gamma_o$ ) and longitudinal displacement angle of the contact patch ( $\varsigma$ ).

In that Ref., the normal force on the outer and inner wheel in relation to a curve ( $N_e$  and  $N_i$ , respectively) have been obtained and later decomposed in their perpendicular and parallel

components ( $N_{\perp}$  and  $N_{\parallel}$ ). It should be noted that a straight section,  $N_e$  and  $N_i$  would be identical ( $N$ ). The process is summarized in Figure 10 and the resulting formulae are shown underneath it:

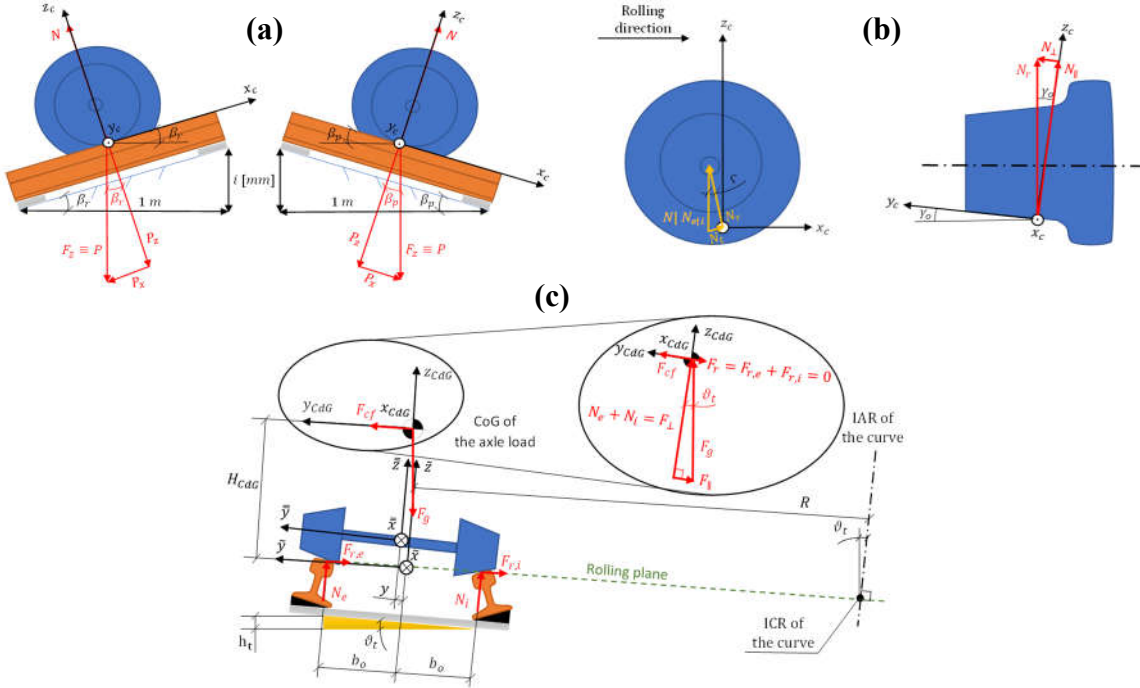


**Figure 10.** (a) Force diagram when the gradient is positive (left) or negative (right); (b) Normal force components at the contact area; (c) Force diagram of a wheelset negotiating a canted curve. Source: Own elaboration.

$$\lambda_{eje} = \frac{\lambda_u + \lambda_{tara}}{n_{ejes}} \quad (18)$$

$$H_{CdG} = \frac{\frac{1}{n_{ejes}}(\lambda_u H_u + \lambda_{tara} H_{tara})}{\frac{1}{n_{ejes}}(\lambda_u + \lambda_{tara})} \quad (19)$$

$$\beta_{rp} = \arctan\left(\frac{i}{1000}\right) \quad (20)$$

$$\vartheta_r = \arcsen\left(\frac{h_r}{2b_o}\right) \quad (21)$$

$$a_{lat} = \frac{V^2}{R+y} - \frac{h'_r}{2b_o} g \cos\beta_r \quad (22)$$

$$N_e = \frac{\lambda_{eje}}{2} \left(1 + \frac{y}{b_o}\right) g \cos\vartheta_r \cos\beta_{rp} + \frac{\lambda_{eje}}{2b_o} a_{lat} H_{CdG} \quad (23)$$

$$N_i = \frac{\lambda_{eje}}{2} \left(1 - \frac{y}{b_o}\right) g \cos\vartheta_r \cos\beta_{rp} - \frac{\lambda_{eje}}{2b_o} a_{lat} H_{CdG} \quad (24)$$

$$N_{\perp} = N_{e|i} \cos(\varsigma) \cos(\gamma_o) \quad (25)$$

$$N_{\parallel} = N_{e|i} \cos(\varsigma) \sin(\gamma_o) \quad (26)$$

#### 2.4.6. Solution of the Geometric and Normal Contact Problems

An isolated wheel transmits its own weight and its load to the rail, with which it shares an interface: the contact area. The contact area must be greater than zero in order to avoid an infinite normal stress. Both the contact area and the normal stress must be determined so as to compute the wear and know where it acts. The first unknown is the geometric problem, whereas the second one is the normal contact problem.

As explained in Ref. (Sichani, 2016), whenever two bodies make contact, that contact can be non-conformal or conformal. In the first type of contact, the contact area is relatively small in comparison with the characteristic size of the bodies; while in the second type of contact, the geometry of a body adapts to the geometry of the other body, resulting in a relatively big contact area (this could happen when the wheel and rail are so worn-out that their geometries coincide).

Ref. (Sichani, 2016) also explains that if the materials in contact are quasi-identical, then the problem becomes much simpler. Quasi-identity implies that a relation between the shear modulus and the Poisson's ratio must be satisfied and in the case of wheel – rail contact, this condition is fulfilled because the materials in contact are the same (steel).

Both the geometric and the normal contact problem are solved together, and in Refs. (Ortega, 2012), (Rovira, 2012) and (Sichani, 2016), these theories for solving them are commented upon:

- Hertzian contact theory: This theory was the first satisfactory analysis for the stresses appearing at the contact zone between 2 elastic solid bodies and solves the geometric problem at the same time if a series of hypotheses are fulfilled. According to this theory, the contact area is the intersection of two perfect paraboloids: a perfect ellipse.
- Kik – Piotrowski theory: This is a quasi-Hertzian theory and is also based on the virtual interpenetration between surfaces. It assumes the same pressure distribution in the longitudinal direction as Hertz, but not in the lateral direction as the curvature is not always constant in that direction. It is interesting to point out that this theory disregards the real shape of the bodies and replaces them by elastic half-spaces, which allows employing Boussinesq's influence functions.
- Ayasse – Chollet: This is also a quasi-Hertzian theory, a variant of the previous one.
- Stiff approach: This theory is based on a stiff contact in which there is a theoretical contact point for which a series of constraints are imposed.

As stated in Ref. (Pellicer & Larrodé, 2021), which collects the theories, the Hertzian contact theory is the most common due to its high accuracy, low computing effort and because the hypotheses it brings are fulfilled for most of the cases. Here is the list:

1. The bodies in contact are homogeneous, isotropic and linear elastic.
2. Displacements are supposed to be infinitesimal (much smaller than the bodies' characteristic dimensions).
3. The bodies are smooth at the contact zone, that is, without any roughness.
4. Each body can be modeled as an elastic half-space, which requires a non-conformal contact.
5. The bodies' surfaces can be approximated by quadratic functions in the vicinity of the maximum interpenetration point. This implies that the curvatures (the second derivatives of the functions) are constant.
6. The distance between the undeformed profiles of both bodies at the maximum interpenetration point can be approximated by a paraboloid.
7. The contact between the bodies is made without friction, so only normal pressure can be transmitted.

In Figure 11, the most representative images of this model are presented. After that, the main formulae are shown, which come from the aforementioned Refs. and also from (Cooper, 1968), (Greenwood, 2018) and (Hertz, 1882):

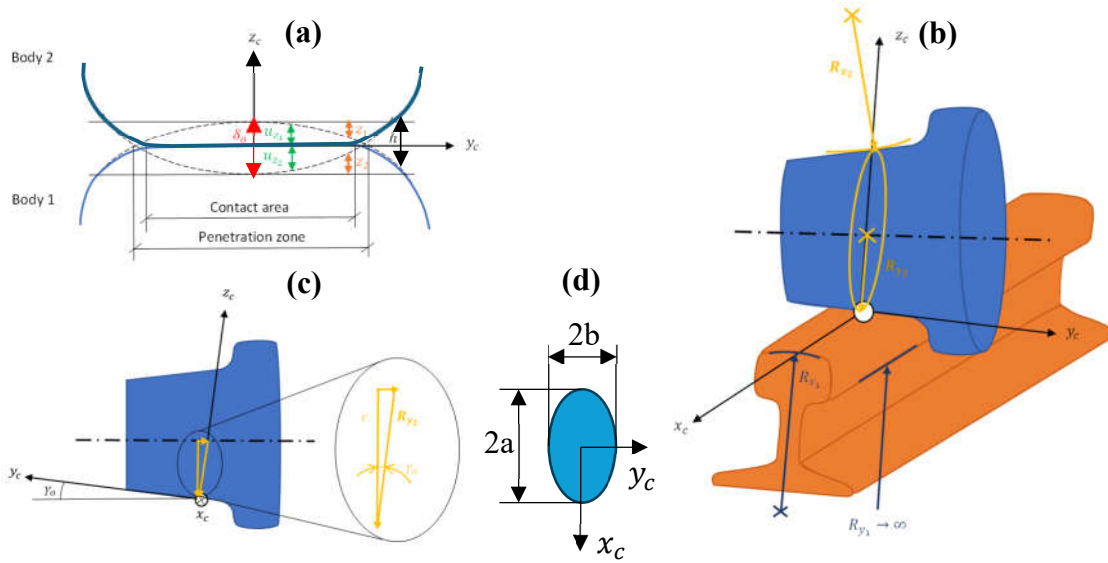


**Figure 11.** (a) Interpenetration between 2 bodies in contact; (b) Graphical representation of the radii involved; (c) Cross-section of the wheel, where  $R_{y_2}$  can be computed; (d) Contact patch with its axes placed. Source: Own elaboration.

$$A = \frac{1}{2} \left( \frac{1}{R_{y_1}} + \frac{1}{R_{y_2}} \right) \quad (27)$$

$$B = \frac{1}{2} \left( \frac{1}{R_{x_1}} + \frac{1}{R_{x_2}} \right) \quad (28)$$

$$R_{y_2} = \frac{r}{\cos \gamma_0} \quad (29)$$

$$A_c = \pi a b \quad (30)$$

$$a = m_H \left( \frac{3}{2} N \frac{1-\nu^2}{E} \frac{1}{A+B} \right)^{\frac{1}{3}} \quad (31)$$

$$b = n_H \left( \frac{3}{2} N \frac{1-\nu^2}{E} \frac{1}{A+B} \right)^{\frac{1}{3}} \quad (32)$$

$$\frac{1-\nu^2}{E} = \frac{1}{2} \left( \frac{1-\nu_1^2}{E_1} + \frac{1-\nu_2^2}{E_2} \right) \quad (33)$$

$$\cos \theta = \frac{|B-A|}{A+B} \quad (34)$$

$$p_{z_0} = \frac{3F_z}{2\pi ab} \quad (35)$$

$$\delta_o = r_H \left( \left( \frac{3}{2} N \frac{1-\nu^2}{E} \right)^2 (A+B) \right)^{\frac{1}{3}} \quad (36)$$

#### 2.4.7. Solution of the Tangential Contact Problem

The Hertzian model ignores the forces and torques due to friction: as a consequence of the relative motion between the wheel and the rail in the longitudinal and lateral directions and around

the vertical axis ( $z_c$ ), opposing forces and torques appear. These are associated with tangential stresses and deformations at the contact area, specifically at the slip region of the ellipse (split into one stick and one slip region). There are two ways to compute these variables:

- Analytical: The values are globally computed for the whole contact patch. A set of analytical equations are used, and the tangential problem can be decoupled from the geometric and normal ones because non-conformity and quasi-identity are satisfied.
- Finite-element: The values of the variables are locally computed and are added thereafter so as to obtain the global values. For that, the contact patch is meshed.

In the current work, the analytical way is chosen, inasmuch as that it allows tackling the problem with an algorithm which comes to the results at a good accuracy – computational effort ratio.

For the computation of these tangential forces and also the spin torque, a series of models have been proposed throughout the last hundred years. In Refs. (Rovira, 2012), (Sichani, 2016) and (Ortega, 2012), these models are commented upon:

- Carter's theory: This was the first theory ever. Carter coined the term "creepage" as "the ratio of the distance gained by a surface with respect to the other divided by the distance run". He stated that the longitudinal dimension of Hertz's ellipse in the unworn profiles was, in general, greater than the lateral one, but, as a consequence of wear, profiles flattened, giving rise to a uniform-width strip. He assumed that the wheel and rail profiles could be approximated by two parallel-axis cylinders, so the problem was reduced to a plane stress problem, that is, bi-dimensional.
- Johnson's theory: Johnson published the first contact theory for circular contacts. In this theory, the stick region is circle-shaped and it touches the leading edge at a single point, although he later showed that this hypothesis leads to a contradiction: tangential stress does not oppose slip at the slip region adjacent to the leading edge. He also derived relations between creepages that were decreasingly small and tangential forces. Finally, he showed that the spin effect also contributes to lateral force.
- Johnson – Vermeulen's theory: Johnson worked later with Vermeulen and both extended the theory of circular contacts under pure creepage (no spin) conditions to cases of elliptical contact. They used the solution for slipping contacts with microslip derived by Deresiewick for elliptical contact, with the only difference being that the stick region touches the leading edge at a single point with the purpose of reducing the erroneous area for a rolling contact case. However, in this theory there was still a region where the friction law was not fulfilled.
- Kalker's theory: At first, Kalker established a linear relation between the tangential forces and decreasingly – small creepages. At such a restrictive situation, it is possible to assume that the whole contact area is in adhesion (there is no slip region). This first linear theory was also known as "non-slip theory" in which the friction law and the friction coefficient were discarded. Due to the lack of saturation of this theory (Coulomb – Amonton's law would be the only saturation), this theory was improved with linear and cubic saturation approaches (CONTACT and SHE methods, respectively).
- Polach's theory: Even with the improvements, Kalker's theory was not enough for computing the lateral tangential force accurately when the spin grows beyond a certain threshold. Polach proposed a method to tackle this problem: (1) Tangential forces computation considering null spin. (2) Tangential forces computation considering pure spin. (3) Addition of the forces computed in steps (1) and (2) and saturation according to the traction limit. For this method, Polach assumed that the ellipse semi-axis in the rolling direction ( $a$ ) tends to zero, so the position of the spin center tends to the ellipse center. He extended this assumption to higher semi-axes ratios ( $a/b$ ).

Ref. (Pellicer & Larrodé, 2021) collects all of these theories and concludes that Polach's method is the most appropriate for considering the spin effect on the variables, inasmuch that it brings accurate results with a low computational effort. Refs. (Polach, 2000) and (Polach, 2005) provide more details on the method.

In Figure 12, the evolution of the stick and slip regions at the contact patch for a case of pure longitudinal creepage is shown, as well as the four contact patches appearing at a four-wheeled bogie without flange – rail contact. At these contact patches, all of the possible creepages, forces and torques

are illustrated. Underneath the figure, the most representative formulae of Polach's method are shown. It must be noted that, for calculations with a variable friction coefficient, the coefficient  $k_A$  is introduced in order to correct the slope of the traction curve:

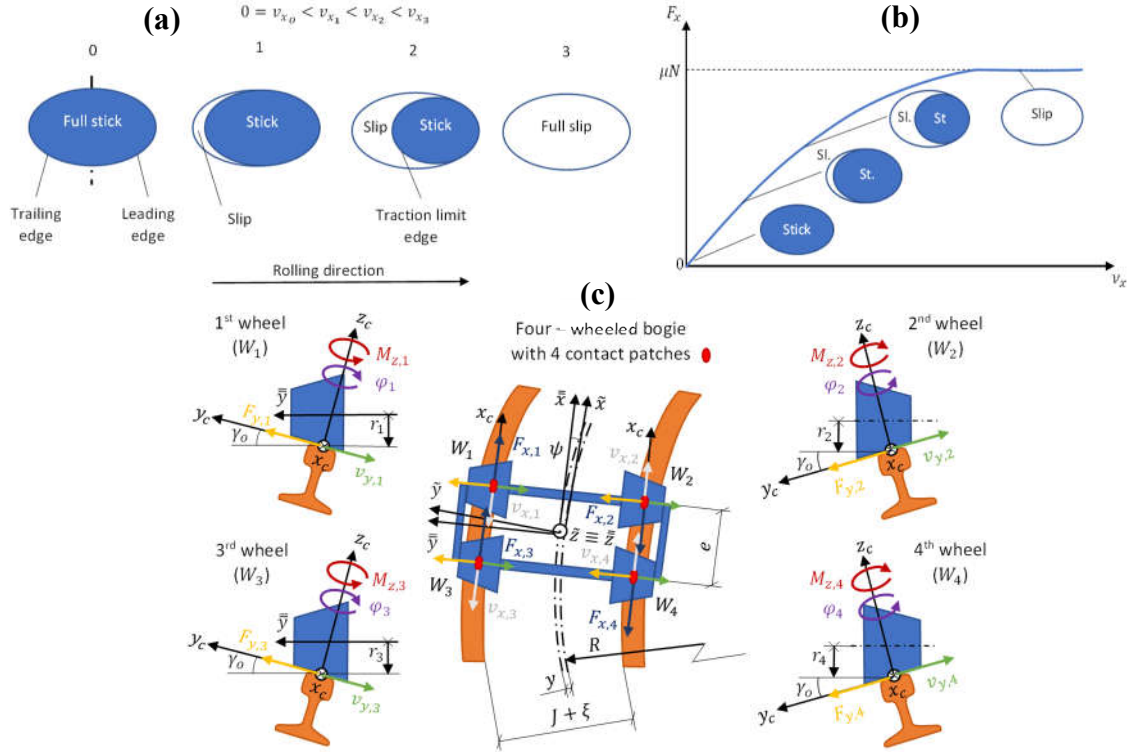


**Figure 12.** (a) Evolution of slip and stick regions as the creepage, purely longitudinal here, grows; (b) Traction curve for the case of pure longitudinal creepage; (c) Tangential forces and torques for a four-wheeled bogie. Source: Own elaboration.

$$s_i = \frac{\mu N_{\perp}}{G a b c_{jj}} v_i, \quad i, j = x, 1; \quad i, j = y, 2 \quad (37)$$

$$\begin{cases} s_{y,C} = s_y + (-\varphi)a, & |s_y + (-\varphi)a| > |s_y| \\ s_{y,C} = s_y, & |s_y + (-\varphi)a| \leq |s_y| \end{cases} \quad (38)$$

$$F = -\frac{2\mu N_{\perp}}{\pi} \left( \frac{\varepsilon}{1+\varepsilon^2} + \arctan \varepsilon \right) \quad (39)$$

$$F_i = F \frac{s_i}{s}, \quad i = x, y \quad (40)$$

$$F_{y,S} = -\frac{9}{16} a \mu N_{\perp} K_M \left[ 1 + 6,3 \left( 1 - e^{-\frac{a}{b}} \right) \right] \frac{(-\varphi)}{s_C} \quad (41)$$

$$F_{y,C} = F_y + F_{y,S} \quad (42)$$

$$F = -\frac{2\mu N_{\perp}}{\pi} \left( \frac{k_A \varepsilon}{1+(k_A \varepsilon)^2} + \arctan(k_S \varepsilon) \right) \quad (43)$$

$$\mu = \mu_o \left[ (1 - A_f) e^{-w B_f} + A_f \right] \quad (44)$$

$$w_i = s_i V \quad i = x, y \quad (45)$$

#### 2.4.8. Characterization of Flange – Rail Contact

Flange – rail contact is an aggressive contact appearing at tight / narrow curves where gauge widening is not enough for a smooth curve negotiation. In this type of contact, the wheel flange presses laterally against the rail and the rail exerts a reaction force on the wheel, which increases the pressure on a region with small radii: the flange. When flange – rail contact exists, the usual tread – rail contact does not cease to exist (at least under the hypotheses here considered), so it is important to know how much loaded is each contact.

For finding the reaction that the rail exerts on the flange, Ref. (Andrews, 1986) proposes the center of friction model. This model states that every bogie, when curving, has a point at which, if a wheel were mounted there, this wheel would spin ideally, that is, with no slip. This point is called the center of friction and determining it allows computing the forces exerted by the rail on the flange – rail contact through force and torque balances.

According to this model, there can be one flange – rail contact (free motion) or two flange – rail contacts (restricted motion). The latter occurs at the tightest curves when the two wheels of a diagonal touch the rails.

As for the load distribution on each contact, Ref. (Piotrowski & Chollet, 2005) explains the Sauvage model. This model considers that the total indentation ( $\delta_o$ ) can be expressed as the sum of the indentation at the tread – rail contact ( $\delta_{br}$ ) and that at the flange – rail contact ( $\delta_{pe}$ ). As these depend on the normal force, it is possible to clear out the normal force on the tread contact ( $N_{br}$ ) and the flange contact ( $N_p$ ). However, this method is heuristic if a powerful finite-element method is not used in order to determine the magnitudes of  $\delta_{br}$  and  $\delta_{pe}$ .

Ref. (Pellicer & Larrodé, 2021) collects both models and simplifies the Sauvage model by introducing the load distribution coefficient ( $\alpha_{fn}$ ), which ranges from 0.5 (same normal load for both contacts) and 1 (the tread contact would become discharged). The usual values for this coefficient are taken from the results of the Sauvage model: 0.7 – 0.8.

Figure 13 illustrates the parts of the center of friction model. It can be noted that the motion is restricted when both the wheels  $W_1$  and  $W_4$  touch the rail, receiving the reactions  $\zeta_{h,1}$  and  $\zeta_{h,4}$  from the rails, respectively. Otherwise, when the motion is free, only the wheel  $W_1$  touches the rail and  $\zeta_{h,4}$  is null. Below the figure, the main equations of this model and the normal force distribution by means of  $\alpha_{fn}$  are presented:

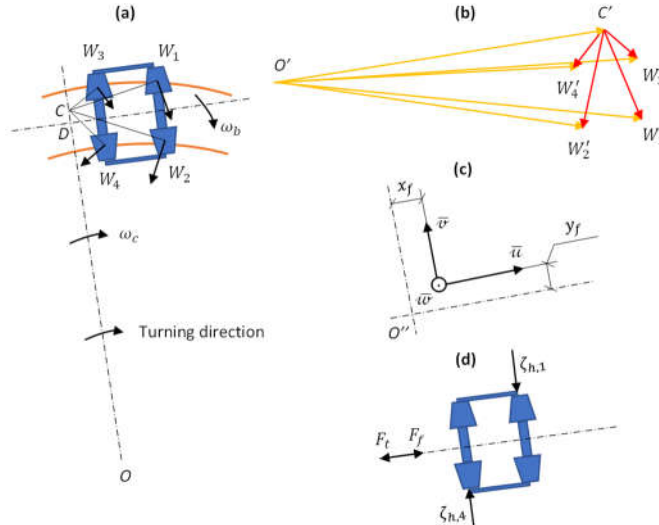


**Figure 13.** (a) Curve negotiation by a bogie; (b) Velocity vectors; (c) Reference frame  $\bar{u}\bar{v}\bar{w}$ ; (d) Forces involved when curving. Source: Own elaboration.

$$\zeta_v = \alpha_{fn} N_e \quad (46)$$

$$N_p = \zeta_v \cos\gamma_o + \zeta_h \sin\gamma_o \quad (47)$$

$$(-F_t|+F_f) = -\sum_{i=1}^{i=Z_w+2} F'_{x,i} \quad (48)$$

$$\zeta_{h,1} - \zeta_{h,Z_w} = \sum_{i=1}^{i=Z_w+2} F'_{y,i} \quad (49)$$

$$\zeta_{h,1} u_{fl,1} - \zeta_{h,Z_w} u_{fl,4} = \sum_{i=1}^{i=Z_w+2} (F'_{y,i} u_{f,i}) + \sum_{i=1}^{i=Z_w+2} (F'_{x,i} v_{f,i}) \quad (50)$$

#### 2.4.9. Calculation of Wear

Wear is the damage to the wheels which reduces their useful life drastically. This wear is due to abrasive and adhesive wear and there exist models based on a wear rate which enable obtaining the wear depth and, hence, characterizing the damage (Sichani, 2016). Abrasive wear is due to the relative movement between the wheel and rail surfaces and their roughness, which cause friction and this, in turn, the loss of wheel and rail material. In contrast, adhesive wear is due to plastic deformation and to the cohesive forces appearing between both surfaces (Van der Waals, electrostatic or chemical), which ends up producing a material transfer from one surface to the other (González – Cachón, 2017).

For wheel wear characterization, Ref. (Rovira, 2012) listed the following hypotheses:

1. The equations are parametrized for abrasive wear and not for adhesive wear because: (1) Plastic deformation appears, but it is difficult to model without finite-element methods, which come with a high computing cost. (2) It is reasonable to assume that the major contribution is abrasive wear. (3) When the mathematical tools are calibrated with experimental data, both phenomena are already included in the resulting wear law.
2. The different mathematical tools study the wear on the wheel profile, where the wear estimated at every instant is cumulative.
3. Wear is assumed to be regular: the variation of the transversal profile is studied, not pattern formation along the longitudinal (circumferential) direction. Thus, the wear at a certain position and instant is extrapolated to the whole circumference.
4. At the contact interface there are not any pollutants. The effect of pollutants is considering by modifying the friction coefficient or introducing new wear laws.

Considering these hypotheses, the models commented upon in Refs. (Rovira, 2012) and (Sichani, 2016) can be applied to wheel wear characterization:

- Energy transfer models: These models compute the energy dissipated at the wheel – rail interface and associate it with the wear rate, which can be ultimately associated with the wear depth. There are various models, each with its own wear law: Zoroby's model, which is based on the energy flow; the model developed by the British Railway Research (BRR), which is based on a non-continuous wear law depending on the wear regime (mild, transition, severe); and the model developed by the University of Sheffield (USFD), which is based on a continuous wear law divided into several regimes (mild, severe, catastrophic).
- Reye – Archand – Khruschchov (RAK) model: This is the simplest model and characterizes the abrasive wear appearing at the slip zone of the contact area. In this model, the volume of material lost is expressed as function of the slip speed, normal force, hardness of the wheel material (steel) and a coefficient coming from a wear chart divided in wear zones depending on the normal pressure and the slip speed.

In Ref. (Pellicer & Larrodé, 2021), energy transfer models and the RAK model are collected and assessed. The RAK model is hard to implement because it requires a high computational accuracy: if pressure or slip speed is miscalculated, then the RAK coefficient may be wrong and be in another order of magnitude. As to the energy transfer models, the one with an easiest implementation and lowest computational effort is the USFD model since its wear law is continuous, so small errors do not lead to great errors in the end.

Figure 14 shows the wear calculation according to the USFD, which can be eliminated by reprofiling when its depth reaches a certain threshold (Alba, 2015), (Peng et al., 2019), (RENFE, 2020). The main equations of the USFD model are presented thereafter; the wear rate ( $W_{R,USFD}$ ) for the mild, severe and catastrophic regimes as a function of the wear index ( $T\gamma/A_c$ , with  $A_c$  expressed in  $[\text{mm}^2]$ ) and the wear depth ( $H_{USFD}$ , expressed in  $[\mu\text{m}]$ ):

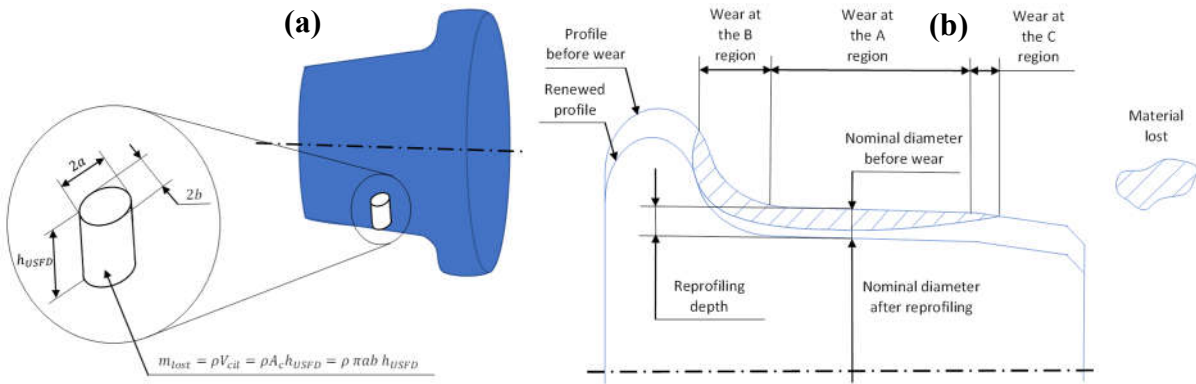


**Figure 14.** (a) Obtention of the wear depth per revolution ( $h_{USFD}$ ); (b) Wheel reprofiling process.  
Source: Own elaboration.

$$\frac{T\gamma}{A_c} = \frac{|F_x v_x| + |F_y v_y| + |M_z \varphi|}{A_c} \quad (51)$$

$$\begin{cases} W_{R,USFD} = 5.3 \frac{T\gamma}{A_c}, \text{ for } \frac{T\gamma}{A_c} \leq 10.4 \\ W_{R,USFD} = 55.0, \text{ for } 10.4 < \frac{T\gamma}{A_c} \leq 77.2 \\ W_{R,USFD} = 55.0 + 61.9 \left( \frac{T\gamma}{A_c} - 77.2 \right), \text{ for } \frac{T\gamma}{A_c} > 77.2 \end{cases} \quad (52)$$

$$H_{USFD} = W_{R,USFD} \frac{a L_{rr}}{\rho \pi r_{rr}} 10^3 \quad (53)$$

#### 2.4.10. Prediction of RCF

Under high axle loads, the stress distribution around the contact patch may cause fatigue cracks on the wheel surface or inside it. For only predicting if RCF is to appear or not, the fatigue index model developed by (Dirks, Ekberg & Berg, 2015) and presented in (Sichani, 2016) is useful. The fatigue index ( $FI_{suf}$ ) is simply the utilized friction term ( $\mu_u$ ) minus the shakedown limit ( $L_{RCF}$ ) and by comparing its value with zero, 3 situations can be observed:

- If  $FI_{suf} < 0$ , RCF is not enough for initiating cracks since the tangential force is moderated (utilized friction).
- If  $FI_{suf} = 0$ , this is the limit situation. Cracks are not initiated as the shear stress at yield ( $\tau_{lim}$ ) has not been reached yet.
- If  $FI_{suf} > 0$ , RCF initiates cracks on the surface since the tangential force is elevated (utilized friction).

The formation of RCF prediction is presented next. The maximum force above which RCF appears ( $F_{max,RCF}$ ) results from equating  $FI_{suf}$  to zero (that is, in the limit situation):

$$FI_{surf} = \mu_u - L_{RCF} \quad (54)$$

$$FI_{surf} = \frac{\sqrt{F_x^2 + F_y^2}}{N} - \frac{\tau_{lim}}{p_{z_0}} \quad (55)$$

$$F_{max,RCF} = \frac{2}{3} \tau_{lim} \pi ab \quad (56)$$

## 2.5. Software Choice

Once the algorithm architecture and details have been defined, it must be implemented in an equation solving program. Due to the large number of input data, equations, relations, functions, procedures and subroutines which had to be implemented, only software capable of processing the entire volume of data in an agile way has been considered. After considering several options (Mathematica, Matlab and Engineering Equation Solver), Engineering Equation Solver (Klein, 1993) has been chosen as it allows building algorithms with any architecture, basing on functions, procedures and subroutines defined in F-Chart programming language, which is a variation of Pascal. The program rearranges internally the equations blocks defined by the user, takes the inputs needed for the new blocks and obtains the requested outputs by means of iterations. These results are obtained after an undetermined number of iterations, depending on adjustable stop criteria such as the relative residuals, which can be as low as  $10^{-10}$ , or the limit of iterations. The specific version with which the results were obtained is Engineering Equation Solver Professional V9.457-3D (EES). The chosen program, besides solving algorithms, can create parametric tables and graphs derived from those equations.

## 2.6. Calculation Scenarios

The objective is to calculate the wear as a function of operating factors such as the nominal diameter for various wheels and compare the results. Prior to getting these results, the calculation scenarios and the input data must be set.

In Ref. (Pellicer & Larrodé, 2021), many types of bogies are reviewed and, as it can be seen, those bogies with reduced-diameter wheels need more wheels to take up the same load. This is because reduced-diameter wheels can withstand lower axle loads than ordinary-diameter wheels (obviously, smaller wheels have less material), so more wheels are needed for the same bogie load. Also, the minimum diameter after the reprofiling cycles is more restrictive in reduced-diameter wheels for operating safety reasons.

For the comparison, these commercial bogies, used or proposed on rail motorways, have been chosen:

- Y – 25: This bogie consists of four wheels (thus, it is composed of two wheelsets) and it can take up 45 t in total (22.5 t/axle) at a maximum speed of 120 km/h. The total wheelbase ( $e$ ) is variable and the wheels are braked, in general, by brake shoes. The wheel nominal diameter ( $D$ ) ranges from 920 mm (original, maximum) to 840 mm (operational minimum).
- Saas-z 703: This bogie also consists of four wheels (so two wheelsets) and it can take up 32 t (16 t/axle) at 100 km/h. The total wheelbase ( $e$ ) is variable and the wheels are braked by brake disks. The wheel nominal diameter ( $D$ ) ranges from 680 mm to 630 mm.
- Graz Pauker 702: This bogie is composed of eight wheels (so four wheelsets) and it can withstand 20 t (5 t/axle) at 100 km/h. The total wheelbase ( $e$ ) is variable and the wheel nominal diameter ( $D$ ) ranges from 355 to 335 mm.

These bogies are different each other, but the comparisons should be performed under the same conditions, only excluding the parameter whose influence on wheel wear is to be assessed (the nominal diameter ( $D$ ), in this case). However, comparing the scenarios under the same conditions is not always possible, as explained in Ref. (Pellicer & Larrodé, 2021):

1. Axle load ( $\lambda_{eje}$ ): If a constant axle load value were given for all of the cases, then the wheels would be overloaded in some scenarios, while underloaded in others. On the one hand, some values as high as 22.5 t/axle would be unrealistic and unfeasible for the 680 and 355-mm wheels. On the other hand, some values as low as 5 t/axle would be realistic and feasible, although the smallest wheel (355 mm) would be fully loaded, working at maximum normal pressure and tangential stresses at the tread – rail interface, while the biggest wheel (920 mm) would be barely

loaded, working at low values of those variables. In order to ensure (as much as possible) the same conditions, the axle load generating the same normal pressure is to be chosen. Specifically, the axle load generating a 1,235 MPa normal pressure, given that that is a common maximum value (maximum axle loads usually induce 1,100 – 1,300 MPa on the wheel and the mean value is 1,235 MPa), even if the axle load of the smallest wheel surpasses the manufacturer's limit.

2. Flange radius ( $r_p$ ): It is the addition of the nominal rolling radius ( $r_o$ , which is a half of  $D$ ) and a constant. So  $r_p$  decreases in proportion with  $D$ .

This implies that some of the data will depend on the scenario, that is, on the wheel tackled at each time. These scenario-dependent data are discussed in Ref. (Pellicer & Larrodé, 2021) and displayed in Table 1:

**Table 1.** Specific input values for each of the three scenarios.

Variable	Value for 920-mm wheels scenario	Value for 680-mm wheels scenario	Value for 355-mm wheels scenario
$D$ (m)	0.920	0.680	0.355
$n_{ejes}$ ( $\emptyset$ )	4	4	8
$r_p$ (m)	0.467 – 0.475	0.347 – 0.355	0.185 – 0.193
$\lambda_{eje}$ (kg)	18,784	15,325	6,996

The rest of conditions are the same (for instance, the wheelbase) and are discussed in Subsection 2.7. Only realistic, feasible and plausible values are set and even variations in the geometry and friction are considered (the variation of dry friction with speed).

Taking all of this into account, the three scenarios are established: 920-mm, 680-mm and 355-mm wheels. For each of the scenarios, the input data is entered at first, and then the program runs the algorithm for every stretch of the railway line, switching the direction when the end station is reached. When the wear depth reaches a certain threshold, then the wheel is reprofiled and the scenario execution starts over with a new wheel profile (with a lesser diameter now). After a certain number of reprofiling cycles is reached, the minimum allowed diameter is reached, and the scenario execution ends. All of this is registered in the wheel diameter – mileage curves, which are presented in Section 3.

As for the wear depth threshold, this must be as low as possible for the wheel profiles are not updated as they wear out, so they must be renewed assiduously. A sensible value is 1 mm for the three scenarios (this is not an input value, but rather a stop criterion). The lathe will have to remove a bit more for a right reprofiling: 1.5 mm. Converting this radial data into diametral data, 2 and 3 mm are obtained.

Finally, Figure 15 illustrates the placement of the  $\bar{u}\bar{v}\bar{w}$  reference frame for the bogies (this reference frame is necessary for the center of friction model), the wheels entering a curve first are shown (wheels  $W_1$  and  $W_2$  will be half of the times leading and the other half trailing) and the wheel and rail profiles are geometrically adjusted, paying also attention to the flange – rail contact:

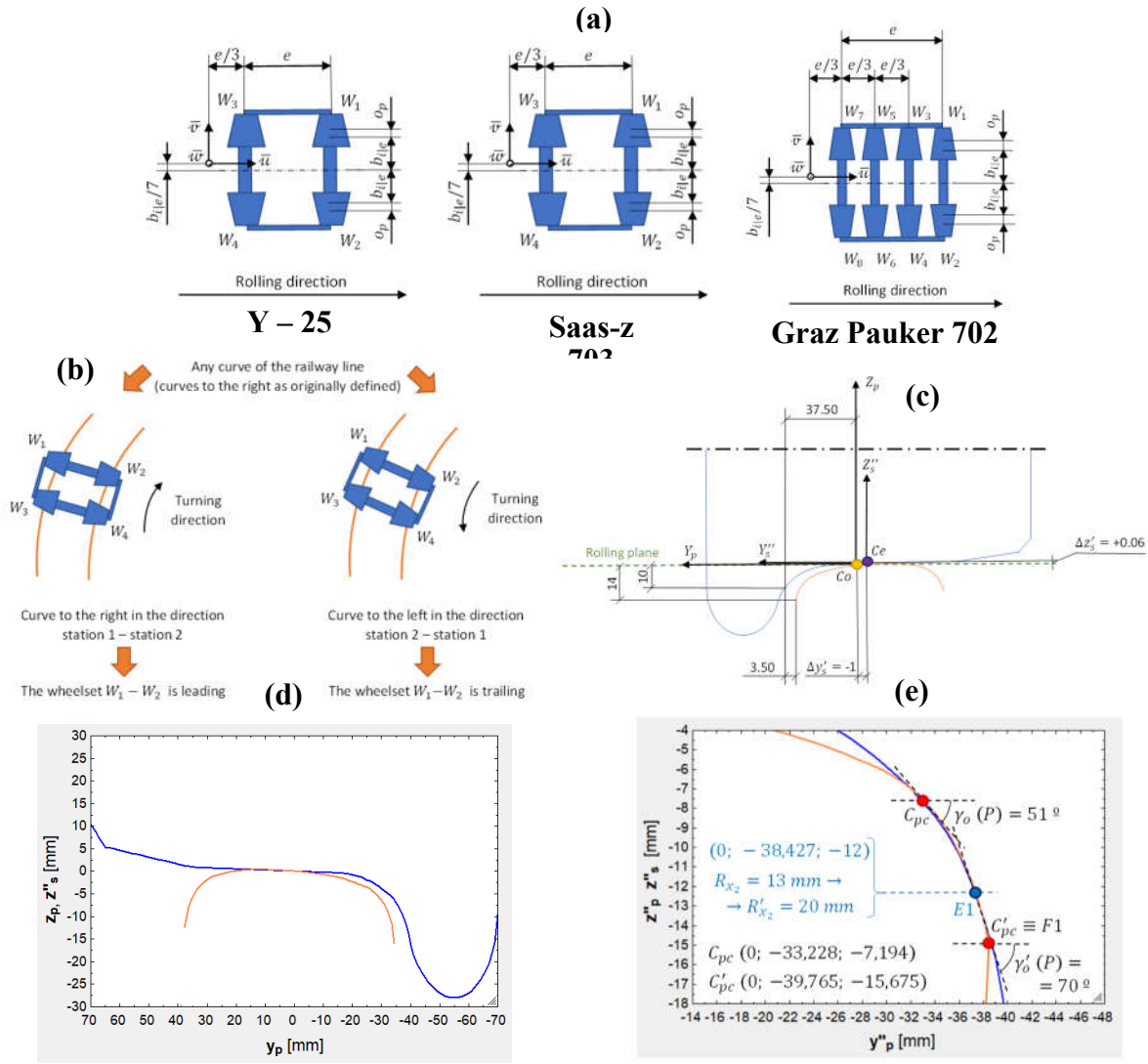


**Figure 15.** (a) Placement of the  $\bar{u}\bar{v}\bar{w}$  reference frame for all the bogies considered; (b) Position of the wheelsets according to the direction; (c) Relative positioning of the right wheel and rail at straight sections; (d) Relative positioning of the left wheel and rail at straight sections; (e) Adjustment between the left flange and rail for wear distribution. Source: Own elaboration.

## 2.7. Input Data

As it can be seen in Figure 3, the algorithm needs to be inputted information relative to the wheelset and bogie geometry, the wheel and rail geometries, the properties of the materials in contact, the load characteristics, the railway line geometry and the vehicle speed. The latter can be associated with the railway line definition if the vehicle runs at the maximum allowed speed associated with the infrastructure.

For the three scenarios, the wheel profile portrays the geometry of the 1/40 standard profile and is made from ER8 steel grade, while the rail profile portrays the geometry of the 60E1 standard profile and is made from R260 steel grade (AENOR, 2011 – 2021). Most of the wheelset and bogie characteristics, which are taken from the bogie comparison carried out in Ref. (Pellicer & Larrodé, 2021) are also common to the three scenarios. The same for the parameters used to modify the friction with speed according to Polach's method (implemented with variable friction under dry conditions). These common input data are shown in Table A3 (Appendix B).

As for the railway line parameters, the calculation is performed for the three scenarios with data from a non-existing railway line. The design parameters of a railway line are defined in Refs. (ADIF,

1983 – 2021), (de San Dámaso, 2011), (Vera, 2016) and (Yassine, 2015), although not all of the parameters are used for wear calculation.

In Ref. (Pellicer & Larrodé, 2021), a railway line is defined stretch by stretch, with these parameters:

- Initial and final metric points ( $Q_{in}$  and  $Q_f$ , respectively).
- Type of stretch: RECTA (straight), CIR (circular curve), CLO (clothoid), PARACUAD (quadratic parabola) or PARACUB (cubic parabola).
- Direction of the curve: NING (the stretch is straight), IZDA (curve to the left) or DCHA (curve to the right).
- Position of the bogie at the curve: NING (the stretch is straight), ENT (the bogie is entering the curve), SAL (the bogie is exiting the curve).
- Curve radius ( $R$ ), cant ( $h_r$ ) and inclination ( $i$ ).
- Initial and final maximum speed allowed ( $V_{in}$  and  $V_{fn}$ , respectively).

Constant values as the track gauge (1.668 m) are the same for all of the stretches, and the gauge widening is a piecewise-defined function which can be directly imported from Ref. (ADIF, 1983 – 2021), which specifies the gauge widening parameter ( $\xi$ ) as a function of the curve radius ( $R$ ). For example,  $\xi$  is null for curves with  $R$  greater than 300 m and  $\xi$  is equal to 20 mm for curves with  $R$  between 100 and 150 m.

Other values as the transition curves parameters are pre-defined and others can be inferred from the values above. For instance, the distance traveled between two metric points is the difference between them.

The 333 stretches defined in Ref. (Pellicer & Larrodé, 2021) can be found in the supplementary material. The curve radii range from a minimum of 265 m (the ratio  $e/R_{min}$  is less than 0.01 and according to this heuristic rule, any restricted movements will appear) to a maximum tending to infinity at straight sections ( $\infty$  is not accepted on EES, so it is assimilated to  $5 \cdot 10^7$ ), with 200 – 800-m radii as the most frequent. It can also be noted that, for more realism, the station 1 is called Albarque, the station 2 is called Zácarín and there is even an intermediate station called Milbello (all of these are fictional names).

Finally, it is noteworthy that the attached material also includes the introduction strategy of Hertz's and Kalker's coefficients into the analysis through polynomials and the 150 equations which have not been displayed in the present document due to lack of space (they are displayed making part of the algorithm already) (Pellicer & Larrodé, 2024).

### 3. Results

After executing the algorithm, the diameter – mileage curves are obtained. Here, the diameter is expressed in [mm], whereas the distance traveled is in [km]. The results are discussed in Section 4, but some numbers can be anticipated:

1. 920-mm wheels can travel for 124,275 km until reaching an 840-mm diameter, losing 2 mm in diameter at every reprofiling cycle. At that point, the worn-out profile will be discarded for safety and operational reasons.
2. 680-mm wheels are able to travel for 75,648 km until reaching their minimum allowed diameter: 630 mm. This is the real life end for this wheel, yet the wear – reprofiling cycles have been extended, as if the final diameter could be 600 mm for the difference between 680 and 600 is the same as that of 920 and 840. In this fictional situation, the wheel would have traveled 118,683 km (fictional life end).
3. 355-mm wheels are capable of traveling 26,983 km until reaching their minimum allowed diameter: 335 mm. This is the real life end for this wheel, yet the wear – reprofiling cycles have been extended, as if the final diameter could be 275 mm for the difference between 355 and 275 is the same as that of 920 and 840. In this fictional situation, the wheel would have traveled 101,433 km (fictional life end).

Besides, a worn-out wheel profile is represented by fitting the wear depths obtained to the zones of a real wheel profile suffering the wear. This wear has been obtained after a random distance

traveled and the coordinates used are the pair  $z_{p,f} - y_{p,f}$  ( $z_{p,f}$  is the vertical coordinate of the final profile, while  $y_{p,f}$  is its horizontal counterpart).

The worn-out profiles shows that the flange wear is far more noticeable and significant than the almost-negligible tread wear, as was expected knowing that flange – rail contact is such an aggressive type of contact and that tight curves are predominant in the railway line defined. In fact, the algorithm determines that in most flange – rail contacts, RCF appears due to the high normal pressures and tangential stresses involved.

Figure 16 displays the three diameter – mileage curves and the worn-out wheel profile, the latter on the lower right corner. As it can be seen on the first plot, the wheel always starts with a 920-mm nominal diameter (at the tread). Right after reaching the wear depth limit (1 mm in radius or 2 mm in diameter, reached at the flange first), the wheel is sent to the workshop for lathing. This process starts with a diameter close to 920 mm at the tread (barely worn-out) and ends with a 917-mm diameter at the tread. Therefore, 3 mm material are removed (1.5 mm in radius, at each side if looked on a cross-section). The wheel exits the workshop with a 917-mm diameter and it wears out until 915 mm, then it is reprofiled from 917 to 914 mm, and so on. Table A5 (Appendix C) should be checked too:

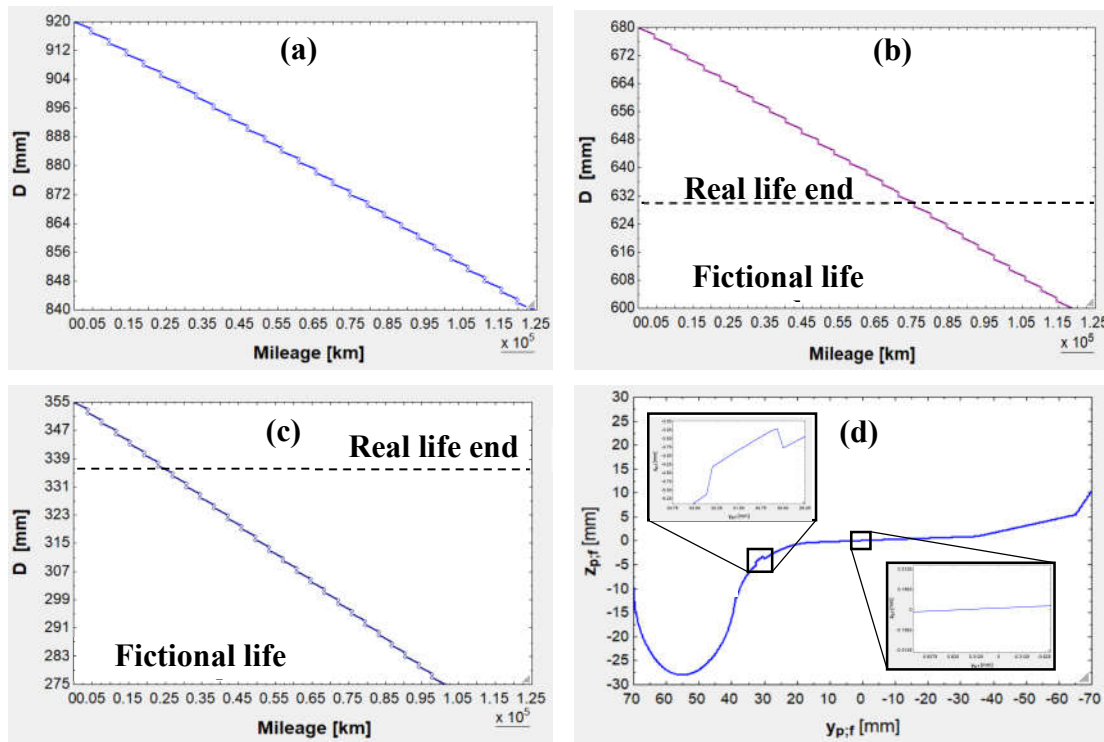


**Figure 16.** (a) Diameter – mileage curve for the 920-mm scenario; (b) Diameter – mileage curve for the 680-mm scenario; (c) Diameter – mileage curve for the 355-mm scenario; (d) Representation of a worn-out wheel profile after a random distance traveled.

#### 4. Discussion

An algorithm capable of calculating wheel wear has been designed in this work. As seen in Figure 16, it has been found that a 920-mm wheel installed on a Y – 25 bogie can travel for 124,275 km, a 680-mm wheel mounted on a Saas-z 702 bogie can travel for 75,648 km, while a 355-mm wheel assembled on a Graz Pauker can travel for 26,985 km. Should the last two wheels undergo the same number of wear – reprofiling cycles as the first one, then their results would be greater than that of the 920-mm wheel: 118,683 and 101,433 km, respectively.

For the understanding of these results, it is necessary to review certain aspects found when analyzing all of the work overall, delving also into the underlying equation blocks which eventually lead to the diameter – mileage curves:

- Comparing the real life ends (124,275; 75,648 and 26,985 km) in percentual terms with respect to the first value, it is obtained that 680-mm wheels' life is 30.13 % shorter and the 355-mm wheels' is 78.29 % shorter.
- Due to the elevated life shortening of 355-mm wheels, operators prefer using bigger wheels. For example, in Ref. (Pellicer & Larrodé, 2021), 380-mm wheels, which are mounted on the Saadkms690 bogie, are presented, which can be reprofiled until reaching 335 mm and the difference between both values (45 mm) is 25 mm higher than for 355-mm wheels (20 mm). Escalating the life of 355-mm wheels heuristically with the ratio 45/20, the result is 43,176 km, only 65.26 % shorter than 920-mm wheels' life. This is very advantageous despite the elevation in 25 mm of the loading plane height, so replacing 355-mm wheels by 380-mm wheels will ultimately depend on the application (semi-trailers' heights and tunnels and bridges' loading gauges).
- The distance difference between reprofiling (the reprofiling span) is very variable when reprofiling a same wheel and, obviously, when moving across wheels, so adopting arithmetic mean values is required. The mean value is 4,603 km for 920-mm wheels, 4,396 km for 680-mm ones and 3,757 km for 355-mm ones.
- Should the wagons perform  $n$  routes Albarque – Zácarín – Albarque (75.272 km) a week, then reprofiling periodicity should be  $\text{Reprofiling span} \cdot (7/(75.272n))$ . Using the average value 4,250 km, the approximate result obtained is  $56 \cdot (7/n)$ .
- If all of the wheels were reprofiled the same number of cycles (always eliminating 80 mm in diameter), then the wheels' life (fictional, as eliminating 80-mm would be against the manufacturers and operators' regulations) would be: 118,683 km for 680-mm wheels and 101,433 km for 355-mm wheels. The former value is 4.50 % lower than that of 920-mm wheels (124,275 km), while the latter value is 18.38 % lower.
- These trends are summarized in Figure 17, where it can be seen that neither the behavior of the real life end nor that of the fictional life end are linear:

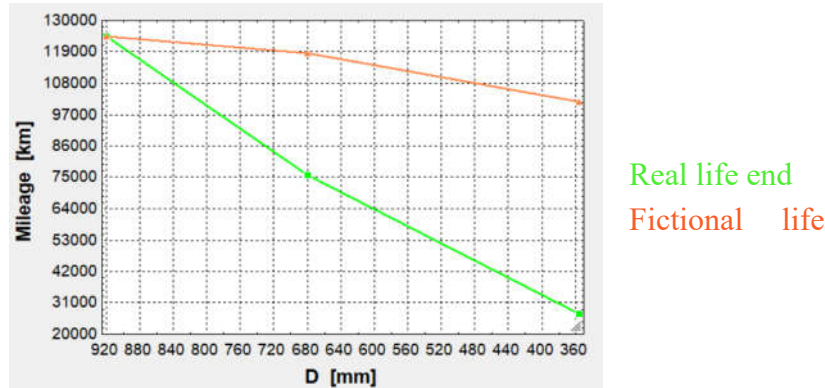
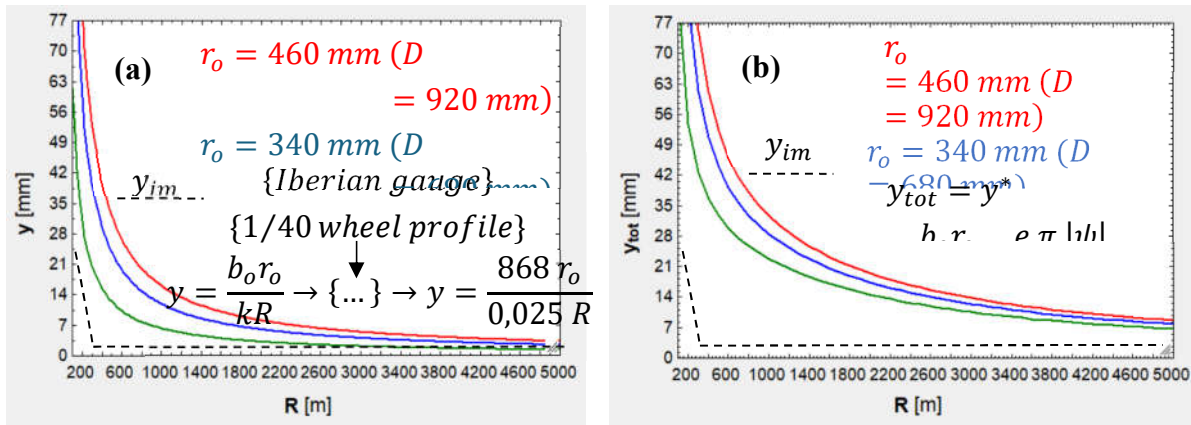


Figure 17. Trends summary.

- This non-linear behavior responds to the different kinematic response of reduced-diameter wheels when negotiating curves. As demonstrated by Redtenbacher's formula, uncentering is proportional to wheel radius (to wheel diameter in turn, as radius is the half), so not only do reduced-diameter wheels uncenter less than ordinary-diameter ones, but also their flanges will push against the rails less intensely. Moreover, the bogies where reduced-diameter wheels are mounted are less loaded, which will further reduce the force exerted by the rail on the flange (coming from force and torque balances). Figure 18(a) illustrates partial uncentering (differential effect) for the three scenarios and shows how saturation ( $y_{lim}$ ) is reached at a lower radius threshold for reduced-diameter wheels, while Figure 18(b) shows total uncentering (adding bogie rotation) in the worst case (leading wheelset, outer wheel), but even in this case, flange – rail contact is less aggressive owing to dynamics:



**Figure 18.** (a) Partial uncentering for different  $r_o$  and  $R$  values; (b) Total uncentering for the same values.

- The results for the three scenarios have been obtained for a 1,235-MPa normal pressure at the tread contact area with the rail when the wheels run on straight tracks, attaining such value by adjusting axle load for each scenario. Pressures existing at the flanges have not been equated due to the variability of the force exerted by the rail on the flange on the curve radius, which would make it very difficult to obtain unique axle load values.
- It is necessary to limit axle load on reduced-diameter wheels, as their contact area with the rail is reduced as well and the normal pressure is proportional to the load – area ratio. This reduction in the contact area responds to the decrease in the longitudinal radius  $R_{y_2}$ , which is proportional to the wheel diameter. With a lower  $R_{y_2}$  value a greater longitudinal relative curvature ( $A$ ) is obtained, which diminishes the intersection between the theoretical paraboloids and, as a result, the contact patch size (as  $A$  diminishes, the longitudinal semi-axis ( $a$ ) does as well).
- Flange wear is between 10 and 1,000 times more intense than tread wear, so the former has been taken for elaborating the curves. This is due to the fact that lateral radii are very reduced for flange – rail contact ( $R_{x_1} = 13 – 36$  mm,  $R_{x_2} = 36$  mm), opposing tread – rail contact radii ( $R_{x_1} = 80 – 300$  mm,  $R_{x_2} \rightarrow \infty$ ), increasing in turn the relative lateral curvature ( $B$ ), which diminishes the intersection between the theoretical paraboloids and, as a result, the contact patch size (as  $B$  diminishes, the longitudinal semi-axis ( $b$ ) does as well). This size is smaller than that of the tread contact patch.
- Wheel diameter is more influential on tread wear than on flange wear. This owes to the fact that the radius  $R_{y_2}$  (proportional to wheel diameter) is dominating, along with the radius  $R_{x_1}$  (which is in the same order of magnitude), at the tread ( $R_{y_2} \sim R_{x_1}$  and  $R_{y_1}, R_{x_2} \rightarrow \infty$ ). In contrast, at the flange,  $R_{y_2}$  is not the dominating radius, being dominated by  $R_{x_1}$  and  $R_{x_2}$  values, which are in a lower order of magnitude ( $R_{x_1} \sim R_{x_2} < R_{y_2}$  and  $R_{y_1} \rightarrow \infty$ ), and  $R_{x_1}$  and  $R_{x_2}$  hold constant independently of wheel diameter.
- RCF is predicted for every flange – rail contact (except for isolated cases where the 355-mm wheel is negotiating a curve with a radius closely below 1,850 m, being this the threshold radius in this case) as a consequence of the high normal pressure (5 – 7 GPa) at the flange contact area with the rail. Although the contact patch size is smaller than that of the tread contact patch, such a high pressure is withstandable by the material since indentation is elevated (0.2 – 0.3 mm) and pressure can stack in many layers (isobaric surfaces), as in hydrostatics.
- RCF effects can be mitigated by setting a reduced wear depth limit and in the current work it has been so due to the hypothesis established. In real operation, it is the economical factor the one prioritized, which forces to find the trade-off between crack growth and wear depth limit.
- As a consequence of RCF and the fatigue induced during reprofiling (which leaves residual stresses) and also for operational safety reasons, operators' internal regulations forbid eliminating more than 80 mm in diameter for a 920-mm wheel, more than 60 for a 680-mm one and more than 20 for a 355-mm one.
- Last, Table A4 (Appendix C) gathers the RCF and wear results for the three different wheels when negotiating the tightest curve, the one with the 265-m radius. As it can be seen, even

though the forces and RCF are less aggressive for reduced-diameter wheels, the wear depth increases as the wheel diameter decreases, for reduced-diameter wheels must revolve more times around its diameter so as to cover the same linear distance. However, the increase in wear depth is not simply inversely proportional to diameter (Figure 17 shows the same non-linear trend).

## 5. Conclusions

Through mathematical modeling, a physical problem as the wear of reduced-diameter railway wheels has been tackled. The algorithm which has been constructed has allowed emphasizing the importance of diameter in the wear problem.

The algorithm constructed interconnects some calculation models and methods by other authors, all of which exhibit good accuracy – computational effort ratios. Moreover, it allows taking into account the main factors impacting wheel wear, some of which are associated with the vehicle (wheel and wagon factors), while others are associated with the superstructure. By introducing boundary conditions and hypothesis complementing those of the calculation models used, the algorithm enables computing the wear with a parametric variation (diameter variation, among others).

In the case presented, wheel wear computations have been utilized for the obtention of diameter – mileage curves for several scenarios: 920-mm diameter wheels used on the Y – 25 bogie, 680-mm diameter wheels used on the Saas-z 702 bogie and 355-mm diameter wheels used on the Graz Pauker 702 bogie. According to the results, when analyzing the evolution of one particular wheel (920, 680 or 355 mm), the wheel degradation worsens as the diameter diminishes, so the reprofiling span shortens as a consequence. This agrees with the initial assumption of the paper: “presumably, reduced-diameter wheels do not undergo the same degradation as the ordinary-diameter wheels due to its greater angular contact with the rail (number of revolutions)”. The results also prove that smaller wheels can travel for shorter mileages than bigger wheels as it was expected.

Notwithstanding, the trend observed when extrapolating the results of 680-mm and 355-mm wheels as though they could be reprofiled as 980-mm exhibits a non-linear behavior. That is, halving the diameter does not imply that the lifespan will halve as well. The comprehension of wheel, wheelset and bogie kinematics and dynamics which this work has enabled, allows finding the root causes responsible for this behavior:

1. Regarding kinematics, reduced-diameter wheels negotiate curves more smoothly than ordinary-diameter wheels, as their uncentering is lower, so their flanges touch the rails less frequently (the threshold radius is lower as well).
2. Regarding dynamics, flange – rail contact is softer. When reduced-diameter wheels' flanges touch the rails, they do it less intensely (uncentering forces are not so intense). Also, the force exerted by the rails on the flange is lower because the bogies based on reduced-diameter wheels are less loaded, so the force and torque balances lead to lower rail – flange forces.

Finally, as a continuation of this research work, a list with the following steps to be carried out is presented:

- Variation of other parameters different from nominal wheel diameter so as to study their influence on wheel wear.
- Reformulation of the algorithm in order to mesh the contact patch and execute calculations globally, including all of the elastic microslips.
- Consideration of conformal contacts, also by means of finite elements as it is not possible to apply Hertz's solution to this type of contacts.
- Addition of rail wear, which would have an impact on wheel wear as the rail curvatures would change (favorably, in general) and the contact positions would differ.
- Update of the contact parameters immediately after the wheel starts to wear out. Clearing out the “wear slope” at every instant would allow for the computation of the actual semi-conicity, contact angle and contact radii.

- Inclusion of the wheel and rail surface roughness, which would require a powerful software, able to characterize surfaces with a micrometric resolution. However, experiments could be performed on unworn profiles, whose roughness is higher.
- Consideration of a different friction coefficient for the tread and the flange since it is not always the same. Flange lubrication could also be considered, trying to optimize the friction value minimizing flange wear at narrow curves.
- Study of the effect of brake shoes on the tread. The shoes would tend to increase tread wheel, yet the overall effect is not very pronounced (the shoes wear out first) and the shoes are also helpful for wiping pollutants off of the wheels (for example, leaves).
- Optimization of the maximum wear depth taking into account economic factors: often reprofiling would lower derailment and crack-failure risks; however, that would come at a high cost, so the trade-off point should be optimized.
- Computation of the speed effects through finite elements, proving more accurate results by obtaining the elastic distortions for every different speed.
- Computation of the exact load distribution between the tread and the flange in the event of simultaneous contacts. Finite elements would allow knowing the real deformations, strains, stresses and forces at both areas.
- Inclusion of more superstructure factors modifying wheel (and rail) wear, such as warp, rail deflection, joints, irregularities and cant excess and deficiency under low static friction conditions.
- Inclusion of impacts between the wheels and the superstructure, especially those of the wheels with the switch frogs and track devices.
- Inclusion of other types of wheel damage shortening wheel life, such as cracks, flats and spalling.
- Extension of the algorithm to cover any other bogies belonging to the wagon (wagons have at least one more bogie).

**Author Contributions:** Conceptualization, D.S.P. and E.L.; methodology, D.S.P.; software, D.S.P.; validation, D.S.P. and E.L.; formal analysis, D.S.P.; investigation, D.S.P.; resources, D.S.P. and E.L.; data curation, E.L.; writing—original draft preparation, D.S.P.; writing—review and editing, E.L.; visualization, D.S.P.; supervision, E.L.; project administration, E.L.; funding acquisition, E.L. All authors have read and agreed to the published version of the manuscript.

**Funding:** This research has been funded through funds from the Transportation and Logistics Research Group of the University of Zaragoza (CITEL).

**Data Availability Statement:** The data presented in this study are contained within the article and supplementary materials in Ref. (Pellicer & Larrodé, 2024).

**Acknowledgments:** This research work is a partial summary of the Master's thesis previously completed by the authors.

**Conflicts of Interest:** The authors declare no conflicts of interest.

## Appendix A

**Table A1.** Latin-symbol abbreviations.

Abbreviation	Definition	Unit (SI)	Abbreviation	Definition	Unit (SI)
$a$	Longitudinal semi-axis of Hertz's ellipse	m	$n_{dec}$	Degree of the function deceleration - time	$\emptyset$
$a_{lat}$	Lateral acceleration experienced by the vehicle	$m \cdot s^{-2}$	$n_{ejes}$	Number of axles on the vehicle	$\emptyset$
$A$	Relative longitudinal curvature	$m^{-1}$	$n'_{ejes}$	Number of axles on the bogie	$\emptyset$
$A_c$	Hertz's ellipse area	$m^2$	$n_H$	Lateral Hertz's coefficient	$\emptyset$
$A_f$	Ratio between the minimum friction	$\emptyset$	$N$	Reaction force of the rail on the wheel on the normal	N

	coefficient (infinite slip speed) and the maximum (null slip)			contact direction (normal force)	
<i>b</i>	Lateral semi-axis of Hertz's ellipse	m	$N_{br}   N_p$	Reaction force of the rail on the wheel in the normal direction to the contact area at the (tread flange) at a wheel experiencing flange – rail contact	N
$b_i   b_e$	Distance from track center to the rolling radius of the (inner   outer) wheel in relation to the curve	m	$N_e   N_i$	Normal force acting on the (outer   inner) wheel in relation to the curve	N
$b_o$	Distance from track center to rolling radius	m	$N_r   N_t$	Normal force component in the radial   tangential direction (the tangential one is perpendicular to the radial one)	N
<i>B</i>	Relative lateral curvature	$m^{-1}$	$N_{\perp}   N_{\parallel}$	Normal force component acting on the wheel (perpendicularly   tangentially) to contact area	N
$B_f$	Exponential constant at friction law	$s \cdot m^{-1}$	<i>o</i>	Existing offset between the track gauge minus the flange – rail play and the distance between the nominal radius center of the wheelset wheels	m
<i>c</i>	Effective size of contact patch	m	$o_p$	Horizontal distance between the center of the flange contact area center and the center of the wheel	m
<i>C</i>	Contact tangential stiffness	$N \cdot m^{-3}$	$p_{zo}$	Maximum contact normal pressure	Pa
$C_s$	Contact tangential stiffness for the pure spin case	$N \cdot m^{-3}$	$Q_i   Q_f$	Initial   final metric point	m
$C_{11} C_{22} C_{11}' C_{22}'$	Longitudinal   lateral   vertical Kalker's coefficient	$\emptyset$	$r_e   r_i$	Theoretical rolling radius of the (outer   inner) wheel in relation to the curve	m
	Kalker's coefficient (longitudinal   lateral)			Rolling radius of the (outer   inner) wheel in relation to the curve including the displacement due to the yaw angle	m
$C'_{11} C'_{22}$	corrected according to non-dimensional slip components	$\emptyset$	$r_e^*   r_i^*$		
$C_{23} C_{32}$	Kalker's coefficients on $y_c z_c$ plane	$\emptyset$	$r_o$	Nominal rolling radius	m
<i>D</i>	Nominal wheel diameter	m	$r_p$	Wheel radius measured until the flange contact patch	m
<i>e</i>	Total bogie wheelbase (measured from its leading to trailing wheelset)	m	$r_{rr}$	Real rolling radius	m

$e'$	Partial bogie wheelbase (measured between 2 next wheelsets)	m	$r_H$	Vertical Hertz's coefficient	$\emptyset$
$E$	Equivalent Young's modulus of the materials in contact	Pa	$R$	Curve radius (measured from its center to the track axis)	m
$E_1   E_2$	Young's modulus of the rail   wheel	Pa	$R_{x_1}$	Rail lateral radius	m
$\delta_i$	Sagitta of the inner rail in relation to the curve	m	$R_{x_2}$	Wheel lateral radius	m
$F$	Magnitude of tangential force vector	N	$R_{y_1}$	Rail longitudinal radius	m
$F_f$	Braking force	N	$R_{y_2}$	Longitudinal wheel radius	m
$F_t$	Traction force	N	$s$	Magnitude of non-dimensional slip vector	$\emptyset$
$F_x   F_y$	Longitudinal   lateral tangential force	N	$s_x   s_y$	Longitudinal   lateral non-dimensional slip	$\emptyset$
$F'_x   F'_y$	Longitudinal   lateral tangential force translated to the reference frame $\bar{u}\bar{v}\bar{w}$	N	$s_c$	Magnitude of non-dimensional slip corrected with the spin contribution	$\emptyset$
$F_{y,c}$	Lateral tangential force (lateral force) corrected with the spin contribution	N	$s_{y,c}$	Lateral non-dimensional slip corrected with the spin contribution	$\emptyset$
$F_{y,s}$	Increase in lateral force due to spin	N	$T\gamma/A_c$	Wear index for the USFD law	$N \cdot m^{-2}$
$F_{máx,RCF}$	Maximum tangential force before rolling contact fatigue appears	N	$u_f$	Coordinate in the $\bar{u}$ axis of the wheel contact area, in the reference frame $\bar{u}\bar{v}\bar{w}$	m
$FI_{surf}$	Fatigue index	$\emptyset$	$u_{fl}$	Coordinate in the $\bar{u}$ axis of the flange outer part, in the frame $\bar{u}\bar{v}\bar{w}$	m
$g$	Gravity acceleration	$m \cdot s^{-2}$	$v_f$	Coordinate in the $\bar{v}$ axis of the wheel contact area, in the frame $\bar{u}\bar{v}\bar{w}$	m
$G$	Equivalent shear modulus of the materials in contact	Pa	$v_{fl}$	Coordinate in the $\bar{v}$ axis of the flange outer part, in the frame $\bar{u}\bar{v}\bar{w}$	m
$G_1   G_2$	Shear module of the rail   wheel	Pa	$v_x   v_y$	Longitudinal   lateral creepage	$\emptyset$
$h_r$	Real cant of the railway line	m	$V$	Vehicle speed	$m \cdot s^{-1}$
$H_{cdG}$	Center of gravity of $\lambda_{eje}$ height over the rolling plane		$V_f   V_i$	Final   initial vehicle speed	$m \cdot s^{-1}$
$H_{tara}$	Center of gravity of $\lambda_{tara}$ height over the rolling plane	m	$w_x   w_y$	Longitudinal   lateral slip speed	$m \cdot s^{-1}$
$H_u$	Center of gravity of $\lambda_u$ height over the rolling plane	m	$w_w$	Wheel width	m

$H_{USFD}$	Total wheel wear depth (USFD law)	m	$W_{R,USFD}$	Wear rate (USFD law)	$\frac{\text{kg}}{\cdot \text{m}^{-1} \cdot \text{m}^{-2}}$
$i$	Railway line gradient / slope	m	$y$	Wheelset uncentering	m
$J$	Track gauge	%	$y^*$	Total wheelset uncentering	m
$k$	Wheel semi-conicity or inclination	m	$y_{lim}^*$	Available play for the bogie leading wheelset when it uncenters towards the outside of a curve	m
$k_A   k_s$	Reduction coefficient for the initial slope of the traction curve at the stick   slip region	$\emptyset$	$y_{lim,diag}^*$	Available play for the bogie trailing wheelset when it uncenters towards the inside of a curve	m
$K_M$	Auxiliary coefficient for the calculation of $F_{y,S}$	$\emptyset$	$\dot{y}$	Wheelset uncentering rate	$\text{m} \cdot \text{s}^{-1}$
$L_{rr}$	Length really rolled by a wheel	N	$\dot{y}^*$	Total wheelset uncentering rate	$\text{m} \cdot \text{s}^{-1}$
$m_H$	Longitudinal Hertz's coefficient	m	$Z_w$	Number of wheels on the bogie	$\emptyset$
$M_z$	Spin torque	$\text{N} \cdot \text{m}$			

**Table A2.** Greek-symbol abbreviations.

Abbreviation	Definition	Unit (SI)	Abbreviation	Definition	Unit (SI)
$\alpha_{fn}$	Fraction of the force normal to the wheel falling on the flange contact patch	$\emptyset$	$\mu_o$	Initial friction coefficient or maximum (null slip speed)	$\emptyset$
$\beta_{rp}$	Gradient angle	rad	$\nu$	Equivalent Poisson's ratio of the materials in contact	$\emptyset$
$\gamma_o$	Wheel contact angle	rad	$\nu_1   \nu_2$	Poisson's ratio of the rail   wheel	$\emptyset$
$\delta_o$	Maximum indentation between the two bodies in contact	m	$\xi$	Gauge widening (at tight curves)	m
$\delta_p$	Auxiliary coefficient for the obtention of coefficient $K_M$	$\emptyset$	$\rho$	Density of the wheel material	$\frac{\text{kg}}{\cdot \text{m}^{-3}}$
$\varepsilon$	Tangential stress gradient at the stick region	$\emptyset$	$\varsigma$	Longitudinal displacement angle of the contact patch	rad
$\varepsilon_s$	Tangential stress gradient at the stick region for the pure spin case	$\emptyset$	$\tau_{máx}$	Maximum tangential stress transmitted	Pa
$\zeta_h   \zeta_v$	Load (horizontal   vertical) on the flange contact patch	N	$\tau_{lim}$	Tangential yield stress of the wheel material	Pa
$\eta$	Play between the flange and the rail	m	$\Phi$	Tilt angle	rad
$\theta$	Hertz's angle	rad	$\dot{\Phi}$	Variation angle of tilt angle	$\frac{\text{rad}}{\cdot \text{s}^{-1}}$
$\vartheta_r$	Real cant angle	rad	$\varphi$	Spin (rotational creepage)	$\frac{\text{rad}}{\cdot \text{m}^{-1}}$
$\lambda_{eje}$	Axle load	kg	$\psi$	Yaw angle	rad
$\lambda_{tara}$	Vehicle tare	kg	$\dot{\psi}$	Variation rate of yaw angle	$\frac{\text{rad}}{\cdot \text{s}^{-1}}$

$\lambda_u$	Payload transported by the vehicle	kg	$\omega'$	Angular slip speed when braking per unit length	rad $\cdot s^{-1}$ $\cdot m^{-1}$
$\mu$	Dynamic friction coefficient (or adhesion coefficient)	$\emptyset$			

## Appendix B

**Table A3.** Input values common to the three scenarios (920, 680 and 355-mm wheels).

Variable	Value	Variable	Value	Variable	Value
$A_f$ ( $\emptyset$ )	0.400	$k$ (flange) ( $\emptyset$ )	1.235 – 2.747	$\gamma_o$ (tread) ( $^\circ$ )	1.432
$B_f$ (s/m)	0.600	$k_A$ ( $\emptyset$ )	1	$\gamma_o$ (tread') ( $^\circ$ )	1.432
$e$ (m)	1.800	$k_S$ ( $\emptyset$ )	0.400	$\gamma_o$ (flange) ( $^\circ$ )	51 – 70
$E_1$ (Pa)	$2.100 \times 10^{11}$	$R_{x_1}$ (tread) (m)	$300 \times 10^{-3}$	$\eta$ (m)	0.007
$E_2$ (Pa)	$2.100 \times 10^{11}$	$R_{x_1}$ (tread') (m)	$80 \times 10^{-3}$	$\lambda_{tara}$ (kg)	20,000
$g$ (m·s $^{-2}$ )	9.810	$R_{x_1}$ (flange) (m)	$13 \times 10^{-3}$	$\mu$ ( $\emptyset$ )	0.400
$G_1$ (Pa)	$81.712 \times 10^9$	$R_{x_2}$ (tread) (m)	$5 \times 10^7$	$\mu_o$ ( $\emptyset$ )	0.550
$G_2$ (Pa)	$81.712 \times 10^9$	$R_{x_2}$ (tread') (m)	$5 \times 10^7$	$\nu_1$ ( $\emptyset$ )	0.285
$H_{tara}$ (m)	0.512	$R_{x_2}$ (flange) (m)	(13 or 20) $\cdot 10^{-3}$	$\nu_2$ ( $\emptyset$ )	0.285
$H_{CdG}$ (m)	1.573	$n_{dec}$ ( $\emptyset$ )	0	$\rho$ (kg·m $^{-3}$ )	7,850
$J$ (m)	1.668	$o$ (m)	0.075	$\tau_{lim}$ (Pa)	$3.120 \times 10^8$
$k$ (tread) ( $\emptyset$ )	0.025	$w_w$ (m)	0.140		
$k$ (tread') ( $\emptyset$ )	0.025	$\alpha_{fn}$ ( $\emptyset$ )	0.750		

**Notes:** (1) Tread' is the tread of the wheel opposed to the wheel experiencing flange – rail contact. (2) Some values are expressed as ranges since flange – rail contact geometry is a little different at every contact. (3)  $5 \cdot 10^7$  means that the value tends to infinity ( $\infty$  is not accepted on EES).

## Appendix C

**Table A4.** Extent of RCF and wear on the three different wheels when flange – rail contact occurs.

Variable	920-mm wheel	680-mm wheel	355-mm wheel
$D$ (m)	0.920	0.680	0.355
$R$ (m)	265	265	265
$F_{surf}$ ( $\emptyset$ )	0.433	0.426	0.409
$p_{z_o}$ (Pa)	$6.401 \times 10^9$	$6.599 \times 10^9$	$6.584 \times 10^9$
$T\gamma$ (N)	468.088	367.463	367.887
$a$ (mm)	10.030	8.249	6.276
$b$ (mm)	0.636	0.611	0.881
$A_c$ (mm $^2$ )	20.031	15.834	17.360
$T\gamma/A_c$ (N/mm $^2$ )	23.368	23.207	21.192
$W_{R,USFD}$ ( $\frac{\mu g}{m \cdot mm^2}$ )	55	55	55
$H_{USFD}$ ( $\mu m$ )	2.295	2.427	3.538
$F_x$ (N)	1274	1034	1009
$F_y$ (N)	41,159	32,931	34,760

$M_z$ (N·m)	197,200	112,100	55,280
$v_x$ ( $\emptyset$ )	$-3.013 \times 10^{-3}$	$-2.917 \times 10^{-3}$	$-2.581 \times 10^{-3}$
$v_y$ ( $\emptyset$ )	$-5.760 \times 10^{-3}$	$-5.760 \times 10^{-3}$	$-5.760 \times 10^{-3}$
$\varphi$ ( $\frac{rad}{m}$ )	1.152	-1.559	-2.986
$N$ (N)	85,465	69,622	76,224

Note: Values for the flange.

## References

1. ADIF. Calificación, geometría, montaje y diseño de la vía; ADIF: Madrid, Spain, 1983 – 2021.
2. ADIF. Declaración sobre la red. Annual Report. 2023. Available online (in Spanish): <https://www.adif.es/sobre-adif/conoce-adif/declaracion-sobre-la-red> (accessed on 15 July 2024).
3. AENOR. Aplicaciones ferroviarias. Ruedas y carriles; AENOR: Madrid, Spain, 2011 – 2021.
4. Alba, M. V. Optimización de la Política de Reperfilado de Ruedas para el Citadis 302, en la explotación de Metro Ligero Oeste. *Revista Vía Libre Técnica* 2015, 9, 29 – 38.
5. Andrews, H. I. Railway Traction. The Principles of Mechanical and Electrical Railway Traction, 1st ed.; ElSevier Science: Oxford, 1986.
6. Bosso, N.; Magelli, M.; Zampieri, N. Simulation of wheel and rail profile wear: a review of numerical models. *Railway Engineering Science* 2022, 30(4), 403 – 436.
7. Cai, W. et al. Experimental and numerical analysis of the polygonal wear of high-speed trains. *Wear* 2019, 440 – 441 (203079).
8. Chunyan, H. et al. A finite element thermomechanical analysis of the development of wheel polygonal wear. *Tribology International* 2024, 195(109577).
9. Cooper, D. H. Tables of Hertzian Contact – Stress Coefficients. Report no. 387 from the Coordinated Science Laboratory. 1968. Available online: <https://core.ac.uk/download/pdf/158319603.pdf> (accessed on 15 July 2024).
10. Dirks, B.; Enblom, R.; Ekberg, A.; Berg, M. The development of a crack propagation model for railway wheels and rails. *Fatigue & Fracture of Engineering Materials & Structures* 2015, 18(12), 1478 – 1491.
11. European Council. Directive 96/53. Official Journal of the European Communities 1996, L 235/59.
12. Fissette, P. Railway vehicle dynamics. Teaching content. Catholic University of Louvain, Louvain. 2016. Available online: <https://es.scribd.com/document/559372304/RailVehicles> (accessed on 15 July 2024).
13. González – Cachón, S. Tribological behavior of micro-alloyed steels and conventional C – Mn in pure sliding condition. PhD Thesis, University of Oviedo, Oviedo, Spain, 2017. Available online (in Spanish): <https://digibuo.uniovi.es/dspace/handle/10651/44961> (accessed on 15 July 2024).
14. Greenwood, J. A. Hertz theory and Carlson elliptic integrals, *Journal of the Mechanics and Physics of Solids* 2018, 119, 240 – 249.
15. Hertz, H. R. Über die Berührung fester elastische Körper. *Journal für die reine und angewandte Mathematik* 1882, 92, 156 – 171.
16. Jaro, L.; Folgueira, C. A. Las Autopistas ferroviarias: ¿Una apuesta de futuro en líneas mixtas de alta velocidad? *Revista de Alta Velocidad* 2012, 2, 73 – 96.
17. Jiménez, P. Ferrocarriles. Teaching content. Polytechnical University of Cartagena. 2016. Available online (in Spanish): <https://ocw.bib.upct.es/course/view.php?id=162&topic=al> (accessed on 15 July 2024).
18. Kalker, J. J. Rolling contact phenomena - linear elasticity, *CISM International Centre for Mechanical Sciences*, 411th ed.; Springer: Vienna, Austria, 2000; Volume 411.
19. Klein, S.A. Development and integration of an equation-solving program for engineering thermodynamics courses. *Computer Applications in Engineering Education* 1993, 1(3), 265–275.
20. Larrodé, E. *Ferrocarriles y tracción eléctrica*, 1st ed.; Editorial Copy Center: Zaragoza, España, 2007.
21. Lyu, K. et al. Influence of wheel diameter difference on surface damage for heavy-haul locomotive wheels: Measurements and simulations. *International Journal of Fatigue* 2020, 132 (105343).
22. Ma, C. et al. The initiation mechanism and distribution rule of wheel high-order polygonal wear on high-speed railway. *Engineering Failure Analysis* 2021, 119(104937).
23. Ministerio de Fomento; Ministère de l’Environnement, de l’Énergie et de la Mer. Servicios de Autopista Ferroviaria (AF) en los ejes Atlántico y Mediterráneo. Convocatoria de manifestaciones de interés. Consulta a los fabricantes y diseñadores de material móvil. Report. 2018. Available online (in Spanish): [https://www.ecologie.gouv.fr/sites/default/files/180410\\_AMI\\_Constructeurs\\_rapport\\_ES-min.pdf](https://www.ecologie.gouv.fr/sites/default/files/180410_AMI_Constructeurs_rapport_ES-min.pdf) (accessed on 15 July 2024).
24. Ministerio de Fomento. Orden FOM/1630/2015, de 14 de julio, por la que se aprueba la “Instrucción ferroviaria de gálibos”. *Boletín Oficial del Estado* 2015, 185.
25. Montenegro, P.A.; Calçada, R. Wheel–rail contact model for railway vehicle–structure interaction applications: development and validation. *Railway Engineering Science* 2023, 31(3).

26. Moody, J. C. Critical Speed Analysis of Railcars and Wheelsets on Curved and Straight Track. Bachelor's Thesis. Bates College, Lewiston, USA, 2014. Available online: <https://core.ac.uk/download/pdf/230689735.pdf> (accessed on 15 July 2024).

27. Oldknow, K. Wheel – Rail Interaction Fundamentals. Course content. 2015. Available online: <https://www.coursehero.com/file/185769149/PC-1-3-Wheel-Rail-Interaction-Fundamentals-WRI-2017-20170604pdf/> (accessed on 15 July 2024).

28. Ortega, E. Simulación del contacto rueda – carril con Pro/ENGINEER, Bachelor's Thesis, Universidad Carlos III, Madrid, España, 2012. Available online (in Spanish): <https://e-archivo.uc3m.es/entities/publication/1ad42047-7a29-4236-a081-52f4c2ec2646> (accessed on 15 July 2024).

29. de Paula Pacheco, P. A. et al. The effectiveness of different wear indicators in quantifying wear on railway wheels of freight wagons. *Railway Engineering Science* **2024**. Available online: <https://doi.org/10.1007/s40534-024-00334-8> (accessed on 15 July 2024).

30. Pellicer, D. S.; Larrodé, E. Analysis of the rolling phenomenon of a reduced-diameter railway wheel for freight wagons, as a function of operating factors. Master's Thesis, University of Zaragoza, Zaragoza, Spain, 2021. Available online (in Spanish): <https://deposita.unizar.es/record/64448> (accessed on 15 July 2024).

31. Pellicer, D. S.; Larrodé, E. Supplementary material of "Analysis of the rolling phenomenon of a reduced-diameter railway wheel for freight wagons, as a function of operating factors". *Mendeley Data*, 3rd version, **2024**. Available online: <https://doi.org/10.17632/xw3hxy5xcx.3> (accessed on 15 July 2024).

32. Peng, B. et al. D. Comparison of wear models for simulation of railway wheel polygonization. *Wear* **2019**, 436 – 437.

33. Piotrowski, J.; Chollet, H. Wheel – rail contact models for vehicle system dynamics including multi-point contact. *Vehicle System Dynamics* **2005**, 43(6 – 7), 455 – 483.

34. Pires, A. C. et al. The effect of railway wheel wear on reprofiling and service life. *Wear* **2021**, 477 (203799).

35. Polach, O. A Fast Wheel – Rail Forces Calculation Computer Code. *Vehicle System Dynamics* **2000**, 33(1), 728 – 739.

36. Polach, O. Creep forces in simulations of traction vehicles running on adhesion limit. *Wear* **2005**, 258(7 – 8), 992 – 1000.

37. RENFE. Temario específico para las pruebas presenciales de la Especialidad Máquinas – Herramientas. Material de estudio. 2020. Available online (in Spanish): [https://www.renfe.com/content/dam/renfe/es/Grupo-Empresa/Talento-y-personas/Empleo/2024/ingenier%C3%ADA-y-mantenimiento/04.%20IYM%20Manual %20Especialidad\\_Maquinas\\_Herramientasv2.pdf](https://www.renfe.com/content/dam/renfe/es/Grupo-Empresa/Talento-y-personas/Empleo/2024/ingenier%C3%ADA-y-mantenimiento/04.%20IYM%20Manual %20Especialidad_Maquinas_Herramientasv2.pdf) (accessed on 15 July 2024).

38. Rincón, L. A. Circulación en curva, esfuerzos y solicitudes verticales en el ferrocarril convencional. Master's Thesis, University of Zaragoza, Zaragoza, Spain, 2018. Available online (in Spanish): [https://eupla.unizar.es/sites/eupla/files/archivos/AsuntosAcademicos/TFG/2013-2014/Civil/convocatoria\\_3/5rincongarcia.pdf](https://eupla.unizar.es/sites/eupla/files/archivos/AsuntosAcademicos/TFG/2013-2014/Civil/convocatoria_3/5rincongarcia.pdf) (accessed on 15 July 2024).

39. Rovira, A. Modelado del contacto rueda-carril para aplicaciones de simulación de vehículos ferroviarios y estimación del desgaste en el rango de baja frecuencia. PhD Thesis, Polytechnical University of Valencia, Valencia, Spain, 2012. Available online: <https://riunet.upv.es/handle/10251/14671> (accessed on 15 July 2024).

40. Salas – Vicente, S.; Pascual – Guillamón, M. Use of the fatigue index to study rolling contact wear. *Wear* **2019**, 436 – 437 (203036).

41. de San Dámaso, R. La vía de tres carriles. Situación actual y perspectivas. Informe de la Dirección General de Operaciones e Ingeniería – Dirección Ejecutiva de Operaciones e Ingeniería de Red de Alta Velocidad. 2017. Available online (in Spanish): <https://cip.org.pt/wp-content/uploads/2017/01/Ref-33.pdf> (accessed on 15 July 2024).

42. Sang, H. et al. Theoretical study on wheel wear mechanism of high-speed train under different braking modes. *Wear* **2024**, 540 – 541 (205262).

43. Santamaría, J.; Vadillo, E. G.; Gómez, J. Influence of creep forces on the risk of derailment of railway vehicles. *Vehicle System Dynamics* **2009**, 47(6), 721 – 752.

44. Sichani, M. S. On Efficient Modelling of Wheel – Rail Contact in Vehicle Dynamics Simulation. PhD Thesis, KTH Institute of Technology, Stockholm, Sweden, 2016. Available online: <https://kth.diva-portal.org/smash/record.jsf?dswid=6030> (accessed on 15 July 2024).

45. Sui, S. et al. Effect of wheel diameter difference on tread wear of freight wagons. *Engineering Failure Analysis* **2021**, 127(105501).

46. Tao, G. et al. Polygonisation of railway wheels: a critical review. *Rail Engineering Science* **2020**, 28(4), 317 – 345.

47. Tipler, P. A.; Mosca, G. *Physics for Scientists and Engineers Vol. I*, 6th ed.; Macmillan Education: London, UK, 2014.

48. Vera, C. Proyecto Constructivo de una Línea Ferroviaria de Transporte de Mercancías y su Conexión a la Red Principal. Bachelor's Thesis, University of Seville, Seville, Spain, 2015. Available online (in Spanish): <https://idus.us.es/handle/11441/44482> (accessed on 15 July 2024).
49. Yassine, B. Los trabajos topográficos en la ejecución de una vía de ferrocarril de alta velocidad. Bachelor's Thesis, Polytechnical University of Valencia, Valencia, Spain, 2015. Available online (in Spanish): <https://riunet.upv.es/handle/10251/54675> (accessed on 15 July 2024).
50. Zeng, Y. et al. An Optimal Life Cycle Reprofiling Strategy of Train Wheels Based on Markov Decision Process of Wheel Degradation. *IEEE Transactions on Intelligent Transportation Systems* **2022**, 23(8).

**Disclaimer/Publisher's Note:** The statements, opinions and data contained in all publications are solely those of the individual author(s) and contributor(s) and not of MDPI and/or the editor(s). MDPI and/or the editor(s) disclaim responsibility for any injury to people or property resulting from any ideas, methods, instructions or products referred to in the content.